Process-Defect-Structure-Property Correlations During Laser Powder Bed Fusion of Alloy 718: Role of *In Situ* and *Ex Situ* Characterizations

S.J. FOSTER, K. CARVER, R.B. DINWIDDIE, F. LIST III, K.A. UNOCIC, A. CHAUDHARY, and S.S. BABU

Components made by laser powder bed fusion (L-PBF) additive processes require extensive trial and error optimization to minimize defects and arrive at targeted microstructure and properties. In this work, *in situ* infrared thermography and *ex situ* surface roughness measurements were explored as methodologies to ensure Inconel® 718-part quality. For a given laser energy of 200 Watts, prismatic samples were produced with different exposure times (80 to 110 μs) and point spacings (80 to 110 μm). The infrared intensities from laser–material interaction zones were measured spatially and temporally. The conditions leading to higher IR intensity and lowest surface roughness values correlated well with less porosity and coarse solidification grain structure. The transition from highly columnar to misoriented growth is attributed to changes in thermal gradients and liquid–solid interface velocities. Hardness measurements and electron microscopy of the as-processed and post-processed heat-treated samples show complex transitions in microstructural states including the heavily dislocated FCC matrix, reduction of dislocation density, and copious precipitation, respectively. These results show that the geometry-process-structure-property correlations are dynamic, and they cascade depending on the transitions of phase states from powder to liquid to solid, as well as phase decompositions and deformations within the solid FCC phase. Validity of using analytical weld process models to describe the above phenomena is also highlighted.

https://doi.org/10.1007/s11661-018-4870-2

I. INTRODUCTION

ONE of the obstacles critical to the adoption of additive manufacturing (AM) is the need for rapid qualification[1,2] of components that includes geometrical conformity, minimal defect density, ideal microstructure, as well as targeted performance requirements through many pathways. First, during the development of AM process parameters, extensive mechanical property (*e.g.*, tensile or fatigue) testing can be performed on standard samples with a given alloy powder and machine. Using the above data and Weibull statistics, the risks of using the same parameters for complex geometry can be forecasted.[3] Second, while manufacturing each and every complex geometry, sacrificial samples with standard geometries for mechanical testing can be made around that component. If the tensile samples meet the target properties, one may assume that the printed component is also qualified in conjunction with existing non-destructive evaluations. Third, extensive amounts of *in situ* measurements[4,5] of thermal signatures,[6–14] geometry,[15,16] and chemistry[17,18] can be performed during the additive manufacturing of components. These *in situ* data can be used in conjunction with selective *ex situ* measurements and integrated computational materials engineering (ICME) principles to predict the expected performance of individual components.[19] The current paper pertains to the validity of this third approach for structural metals and alloys processed by powder bed fusion using laser and/or electron beam energy source. In this paper, we

S.J. FOSTER is with the Department of Materials Science and Engineering, The University of Tennessee, Knoxville, TN and also with Oerlikon AM US, Charlotte, NC. K. CARVER, R.B. DINWIDDIE, and F. LIST III are with the Materials Science and Technology Division, Oak Ridge National Laboratory, Oak Ridge, TN and also with the Manufacturing Demonstration Facility, Oak Ridge National Laboratory, Oak Ridge, TN. K.A. UNOCIC is with the Materials Science and Technology Division, Oak Ridge National Laboratory. A. CHAUDHARY is with Applied Optimization Inc., Dayton, OH. S.S. BABU is with the Department of Materials Science and Engineering, The University of Tennessee and with the Department of Mechanical and Aerospace and Biomedical Engineering, The University of Tennessee, Knoxville, TN 37934 and also the Manufacturing Demonstration Facility, Oak Ridge National Laboratory. Contact e-mail: sbabu@utk.edu

Manuscript submitted May 6, 2018.
Article published online August 14, 2018

evaluated this third approach using Inconel® 718 powders and a laser powder bed fusion (L-PBF) process.[20]

To define the specific scope of the current paper, the existing process flow followed by additive manufacturing practitioners is briefly reviewed. (i) The first step involves, the identification of optimum processing parameters (*e.g.*, laser power, spot size, velocity, hatch distance, and layer thickness) using single track,[21] multiple tracks, and finally followed by layer melting experiments.[22] (ii) Once the layer melting is optimized, standard cubes are made to evaluate the density of parts; (iii) Then, quality of the parts are evaluated by destructive metallographic, as well as, non-destructive X-ray tomography characterizations.[23] (iv) In the next step, standard test samples for mechanical property testing are manufactured and may undergo post-heat treatments (stress relief, hot-isostatic pressing, or machining) and then be tested. (v) Then, the process flow that identified the optimum properties in the test samples will be used for making complex geometry parts. (vi) These components may either go through X-ray tomography or post-process heat treatment, depending upon the application.[24] However, this process flow assumes that the thermal-mechanical signatures, defect distributions, and the microstructural heterogeneities within the complex components are similar to that of samples with simple geometry. The welding literature[25] suggests that the validity of the above assumption may not be correct.

Recently, *in situ* thermal imaging has been used to confirm that the geometry,[26] process parameters,[27] and materials[28] are interlinked when identifying defect generation [29] and microstructural evolution[30] during the electron beam powder bed fusion (E-PBF) process. These measurements were correlated with the background and peak temperatures to define the tendency of porosity formation. In addition, the *in situ* thermal measurements allowed quantitative estimation of the processing conditions that led to the columnar to equiaxed transition (CET) during solidification.[31] However, none of the above research have been integrated and extended to selective laser melting of nickel alloys, or involve an in-depth study of surface roughness, hardness, and microstructure of the melt layers.[32] In addition, none of the published studies provide the comprehensive *in situ* and *ex situ* data from similar processing conditions that may be related to AM benchmark initiatives.[33] The objectives of this paper are to address these two specific gaps.

II. EXPERIMENTATION

A. *Additive Manufacturing Build Preparation*

Matrix of cubes was fabricated with Inconel® 718 powder using the Renishaw® AM250 pulsed laser system. The cubes were fabricated upon support structures to allow for easier separation from the build plate and to minimize dilution from the substrate material. A complete overview of the build parameters, *i.e.*, laser exposure time (Δt_{exp}: 80 to 110 μs; with increments of 5 μs), point-to-point distance (*P2P*: 80 to 110 μm with increments of 5 μm) is illustrated in Figure 1(a). It is important to note that the hatch spacing (HS) is indeed the offset between the *P2P* lines and is therefore the same and will be referred to as point spacing. Nine of the cubes in the matrix were terminated during the build process. This decision was made upon the observation of excessive swelling on the surfaces within the first 50 layers of the parts. This selective termination was necessary to maintain the integrity of the remaining parts and avoid damage to the wiper used for powder recoating. The photograph of the last layer is shown in Figure 1(b) and provides visual cues for the swelling of the surface even with completed builds. Table I provides the overview of all process parameters.

B. *Infrared Imaging*

A FLIR® SC8200 mid-wave infrared (IR) camera, capable of sensing 3 to 5 μm wavelength emission was used. Details of the hardware setup are summarized in Appendix A1. IR images were recorded at a rate of 346.7 Hz with an integration time of 1.245×10^{-3} seconds. The build was imaged through a sapphire window with an estimated transmission value of 88 pct. To avoid excessive amounts of IR data from the build region, the following experimental strategy was used. Upon completion of the cubes, an additional 30 μm powder layer was deposited and two heptagons were melted inside of one another for all the conditions shown in Figure 1(c). The outermost heptagon was displaced 1 mm from any of the edges of the cube and was a single line melt pass for each of the seven sides, while the inner double line melt pass heptagon was displaced from the outer by 1 mm. All displacements were implemented to ensure that the conditions experienced during the single and double melting conditions were consistent in terms of thermal diffusivity boundary conditions expected across the whole layer. Despite the termination of nine cubes, the IR intensity values were measured for all 49 sets of heptagons and their significance will be discussed later.

C. *Surface and Microstructure Characterization*

Surface roughness was measured with a Keyence® VR-3100 at $\times$120 magnification. The top surfaces of all the components, including the heptagon regions, were measured. Each of the cubes was then sectioned down the middle, parallel to the build direction, and characterized using standard optical microscopy techniques. Porosity was measured as a function of build height, stitching together multiple images captured at $\times$50 magnification and analyses were performed using ImageJ®. The Leica® DM4000 microscope was used to measure the width of the single melt pool tracks of the heptagons on the top surface of the completed cubes. Spatial variation of microhardness in the form of maps was measured using LECO AMH55 microhardness tester with 200 g load. Detailed microstructural characterization was performed using a JEOL® 6500F equipped with an EDAX® electron backscatter detector

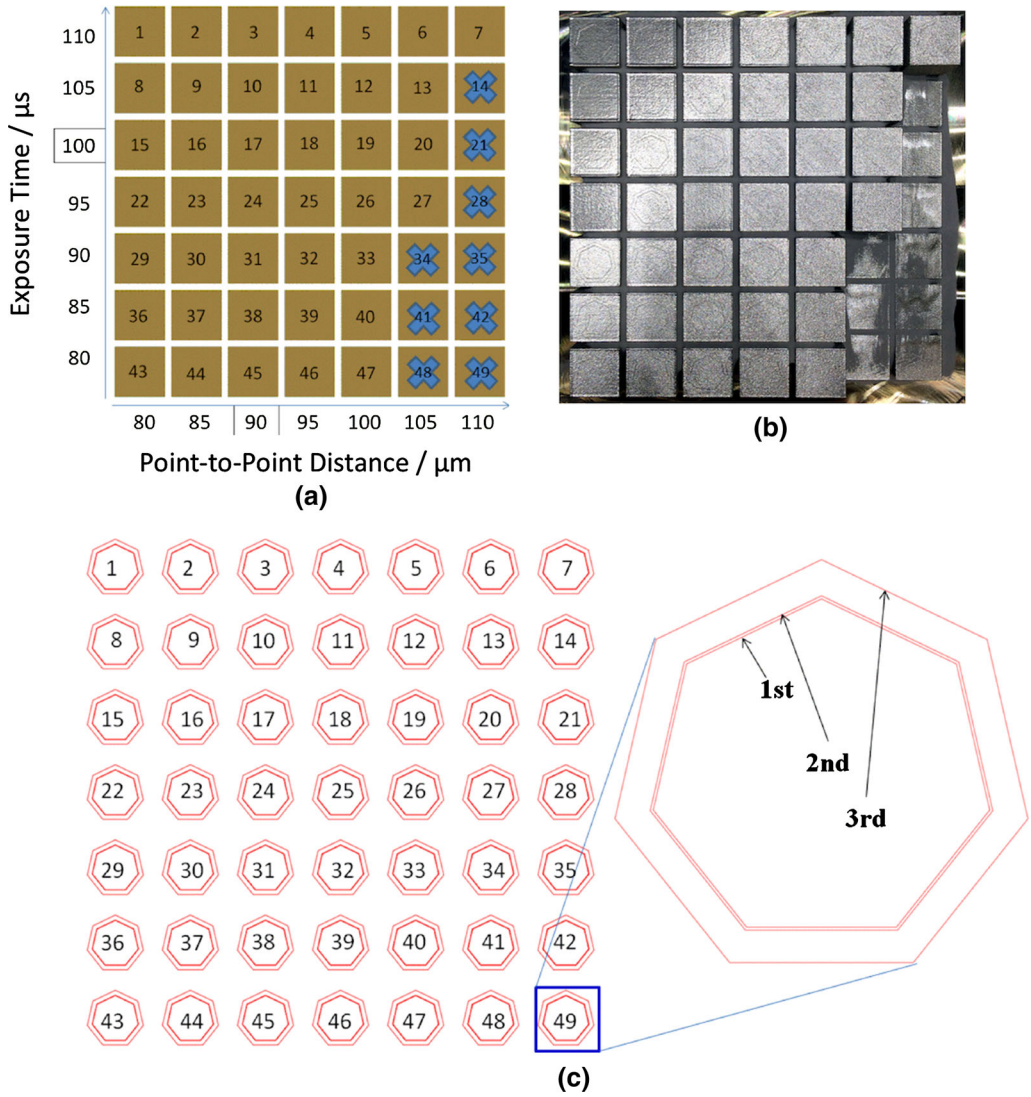

Fig. 1—(*a*) Overview of the process parameters used for the formation of the cubes; (*b*) the photograph of the final surface at the end of the build showing the cubes and also the heptagon geometries; and (*c*) the scan patterns used for the heptagonal geometry made on top of the last layer of the cube surfaces.

Table I. Overview of Process Parameters

Parameters	Values
Power	200 W
Power source	ytterbium fiber laser
Heat source wavelength	1070 nm
Beam diameter	70 μm
Layer thickness	30 μm
Chamber preheat temperature	170 °C
Rotation between layers	67 deg
Cube dimensions	15 mm × 15 mm × 15 mm
Support structure height	6 mm
Melt strategy	meander*

*http://www.renishaw.com/en/design-for-metal-am-a-beginners-guide—42652.

(EBSD). Elemental maps were collected using a Hitachi® S4800 with an EDAX® energy-dispersive X-ray spectroscopy (EDS) detector. The scanning transmission electron microscopy of a few selected samples was performed with Philips CM-200 operated at 200 kV. The reader is referred to other research papers[34,35] to obtain details of different methodologies used for microstructure characterization.

III. RESULTS

A. *Process Feasibility*

As mentioned earlier, among the planned 49 cubes, only forty of them were successfully built. The termination of the nine cubes (*i.e.*, #14, #21, #28, #34, #35, #41, #42, #48, and #49) needs clarification. The decision to terminate was made based on the observation of surface swelling, which occurs due to encasing of unmelted powder particles from the (j − 1)th layer during melting

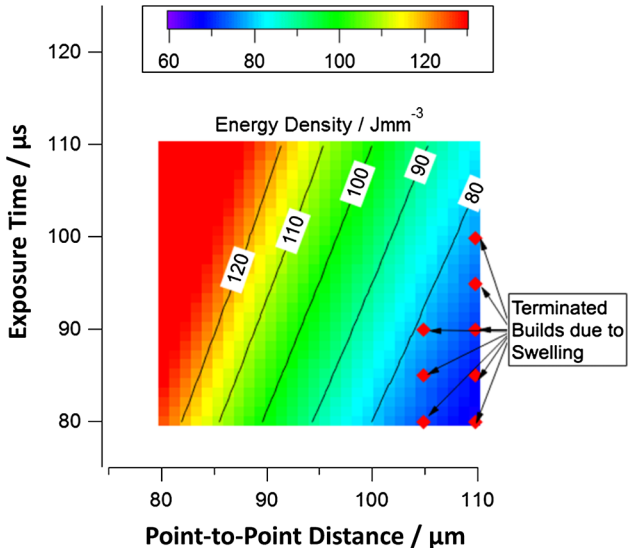

Fig. 2—Image representation of the calculated energy density as a function of exposure time and point spacing, and also the conditions that led to component termination.

of the *j*th layer. Continued processing of these cubes would have led to the impact of these surface protrusions with the motion of the wiper blade during the subsequent layer recoating, and to the eventual disruption of other cubes. This partial melting has been correlated to the volumetric energy density (E_{density}) in the literature. In the following equation, P is the laser power (200 W), HS is the hatch spacing (mm), which is the same as $P2P$, d_{LT} is the layer thickness (30×10^{-3} mm),

$$E_{\text{density}} = \frac{P}{v_{\text{eff}} \times \text{HS} \times d_{\text{LT}}}, \quad [1]$$

and the effective velocity (v_{eff}) in mm/s is calculated with Eq. [2].

$$v_{\text{eff}} = \frac{P2P}{\Delta t_{\text{exp}} + \Delta t_{\text{set}} + \Delta t_{\text{laser}}}. \quad [2]$$

In the above equation, Δt_{exp} is the laser exposure time in seconds, Δt_{set} is the settling time for the laser optics (2×10^{-6} seconds), and Δt_{laser} is the time taken for laser to move from point to point, which has been assumed to be the same and set at 3.6×10^{-5} seconds. It is noteworthy that Δt_{laser} will vary based on the $P2P$, if the velocity of laser deflection is kept constant. The plot of energy density (Figure 2), with the terminated build conditions indicated, shows that there is a critical volumetric energy density (80 J/mm^3) below which the build process will fail. Essentially, below this critical value, the system was unable to recover due to the reduced melt pool depth, which led to excessive trapping of powder particles (lower density), which manifested itself as surface swelling.

B. *In Situ Characterizations*

Infrared measurements during the melting of heptagons on the top surface are best visualized in a movie format to understand the transients. Although, the IR data also captured the spatter formation, this phenomenon was not analyzed due to smearing of the spatter in a given frame because of the limited temporal resolution of the IR camera. Due to the limitation of the printed media, typical data and associated analyses have been uploaded into an online video format.* Typical images from this movie and analyses of the same are shown in Figure 3. It is noteworthy that the IR images were not converted to theoretical temperatures due to the lack of calibration parameters that account for spatial and temporal phase transitions. The phase transitions include changes from powder to liquid and then to solid as the beam traverses the powder bed.[31] The IR intensities were used as a qualitative indicator of the molten pool shape and also the transients in the thermal signatures. The movie, the data, and the analyses confirmed that there was a spatial and temporal variation of the thermal signatures. The peak intensity at each and every location for all of the 49 conditions is summarized in Figure 4.

*https://www.youtube.com/watch?v=hXentP8ocQo.

The infrared data collected from the sets of heptagons (conditions #14, #21, #28, #34, #35, #41, #42, #48, and #49) melted upon pure unsupported powder, mimic 90 deg overhang structures. These conditions led to an increased amount of spatter and ejection of powder particles. This increased spatter and reduced heat condition, due to the lack of solid below the melt regions, resulted in the IR intensities being higher in these areas than any others within the layer. If we ignore the IR data from conditions with point spacing higher than 100 μm, then there are systematic and consistent increases in maximum intensities with decreasing point spacing. This is indeed confirmed by the image plot of minimum, maximum, average, and standard deviation IR peaks as a function of point spacing and exposure time (Figure 5).

C. *Ex Situ Characterizations*

1. *Surface roughness*

The average areal surface roughness was collected from the middle of each of the top layers of the cubes. This information is representative of the instantaneous surface at the *j*th layer before the deposition of the $(j + 1)$th layer or the top surface of the finished component. Typical Keyence surface imaging data are shown in Figure 6(a). The image plot confirmed that most of the surface roughness can be associated with each of the long beads. In certain regions, the contour data (*e.g.*, surface height with 16 μm) showed flat surfaces spanning two adjacent beads, similar to mesas

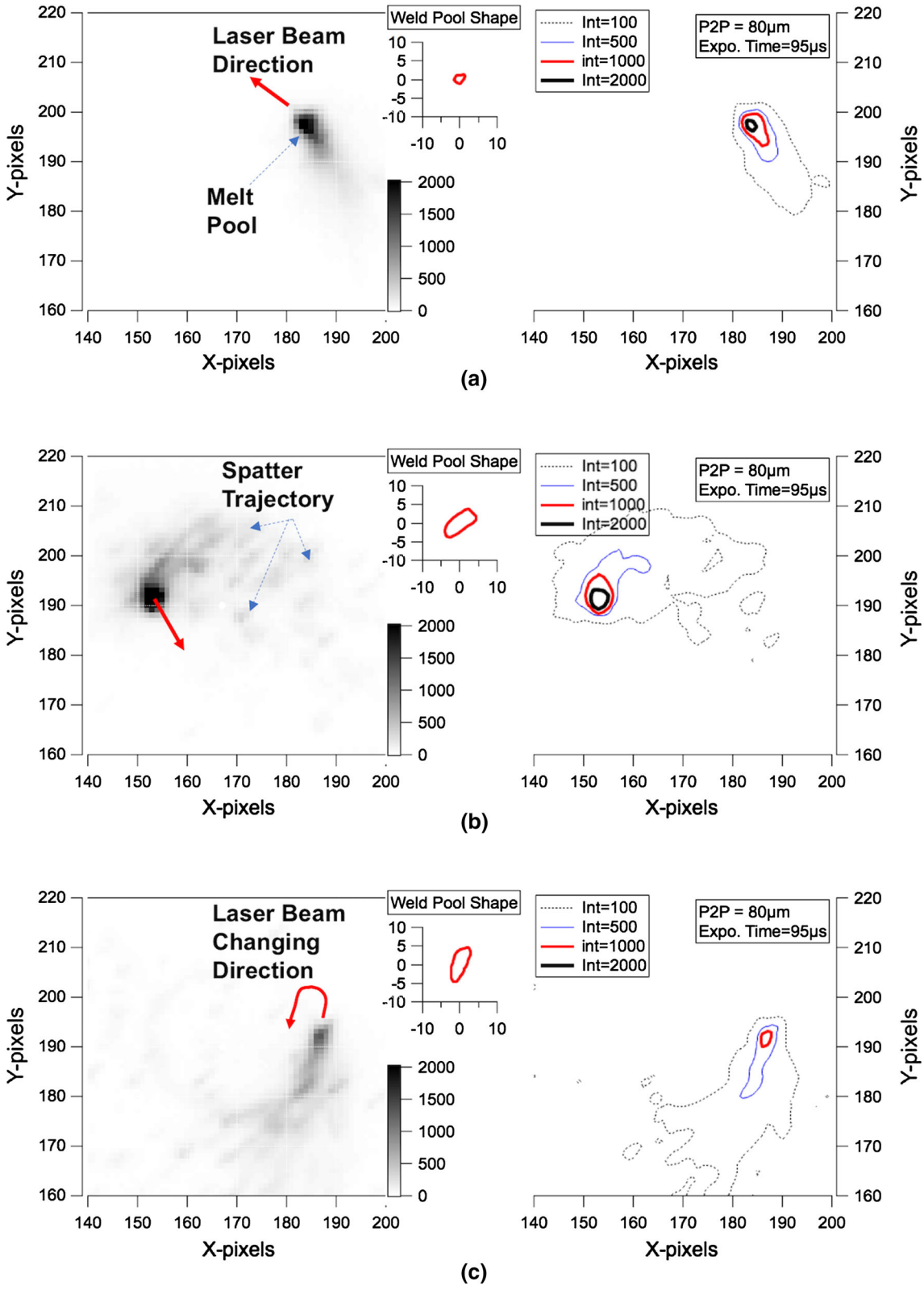

Fig. 3—Snapshots from three different time intervals corresponding to the (*a*) start, (*b*) middle, and (*c*) completion of the heptagon melting on the top surface of the build. The gray scaling and contour plots correspond to different raw IR intensity values.

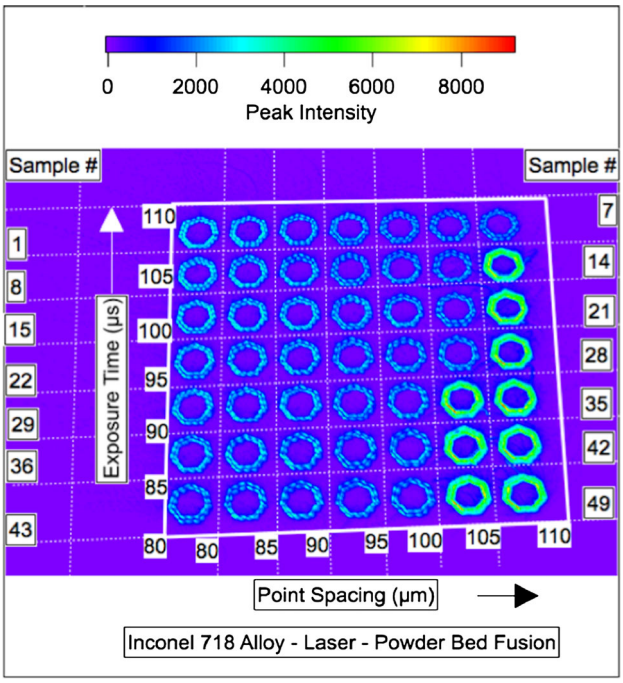

Fig. 4—The maximum peak IR intensities recorded for all of the heptagons melted on the top surface, summarized in an image format.

seen in the mountain ranges. Upon closer examination of all the average surface roughness data, we observed that lowest surface roughness values (Figure 6(b)) correlated with increased volumetric energy density.

2. *Melt-track width and porosity*

In the next step, the single-track melt pool width of the heptagons on the processed surface of the samples (XY plane) were measured using optical microscopy (Figure 7(a)). The above data are also presented in the form of image plot in Figure 7(b). As expected, the long exposure times produced melt pool widths that were larger than the scale of the point spacing. The porosity in the samples was imaged in the (XZ) cross-section (Figure 7(c)) along the depth of the built parts. It is noteworthy to mention that the porosities observed are mostly due to lack of fusion and not due to gas porosity or shrinkage. The above data are also presented in the form of image plot (Figure 7(d)) as a function of point spacing and exposure time.

3. *Solidification microstructure*

Based on the melt pool shapes seen in Figure 7(a), we anticipated that there must be subtle changes in the solidification of crystallographic misorientation, texture with reference to the build direction, and grain size. This was indeed confirmed by the EBSD data shown in Figure 8. The inverse pole images (Figure 8(a)) show that the aspect ratio of the solidification grains changes drastically with an increase in the point spacing. Interestingly, with higher point spacing, the major axes of the columnar grains appeared to change direction with reference to the build direction. This change in orientation with point spacing was also confirmed by the reduction of texture strength of the (001) crystallographic planes along the build direction (Figure 8(b)).

The EBSD data were processed further to extract the size of the grains that were separated by the high-angle grain boundaries (Figure 9). Interestingly, the grain sizes decreased from 50 to 20 μm, with a decrease in exposure time and an increase in point spacing. The dendritic microstructure within these grains was further evaluated with EDS mapping (Figure 10). The EDS maps appeared to be similar with an average primary interdendritic arm spacing of 0.5 μm and subtle, preferential segregations of niobium and oxygen to the interdendritic regions. Although the measurement of oxygen through EDS is unreliable, we have provided this observation due to the strong correlation with underlying dendritic structure.

4. *Mechanical heterogeneity and solid-state transformation*

The hardness maps from selected samples (Figure 11) are presented to evaluate the possibility of solid-state precipitation. Interestingly, the samples processed with small point spacing show large concomitant regions (#9) with 320 VHN (Figure 11(a)), while the samples processed with large point spacing (#47) show smaller regions with 320 VHN (Figure 11(b)) and very soft regions (< 250 VHN). These very soft regions are attributed to the presence of porosity in these samples. The hardness maps from all of the samples were converted into frequency distributions (Figure 11(c)), which revealed that the hardness distributions are consistent across many samples, except for a systematic shift of distributions to lower VHN with decreasing energy density.

Previous research on alloy 718 samples, processed by a direct energy deposition (DED) process, with no solid-state precipitation, only exhibited hardness of 250 VHN. The reason for higher hardness needs to be clarified with transmission electron microscopy (TEM). The sample (#12) with high hardness in the middle region was extracted by focused ion beam machining and characterized *via* TEM. TEM analyses, with electron diffraction and dark-field imaging (Figure 12), failed to show any precipitates; however, extensive amounts of dislocations and sub-grain boundaries were observed. Although not presented, the presence of high dislocation density in the samples was also corroborated with peak broadening in X-ray diffraction analyses when compared to stress-relieved samples. Based on the above results, high hardness is attributed to the formation of fine dislocation cells within the face-centered cubic matrix.

IV. DISCUSSIONS

Recently, there has been a growing need to develop consistent data around AM benchmarking, as well as an increasing focus on evaluating the existing and emerging process-structure-property (PSP) models relevant to additive manufacturing through open challenges.[33]

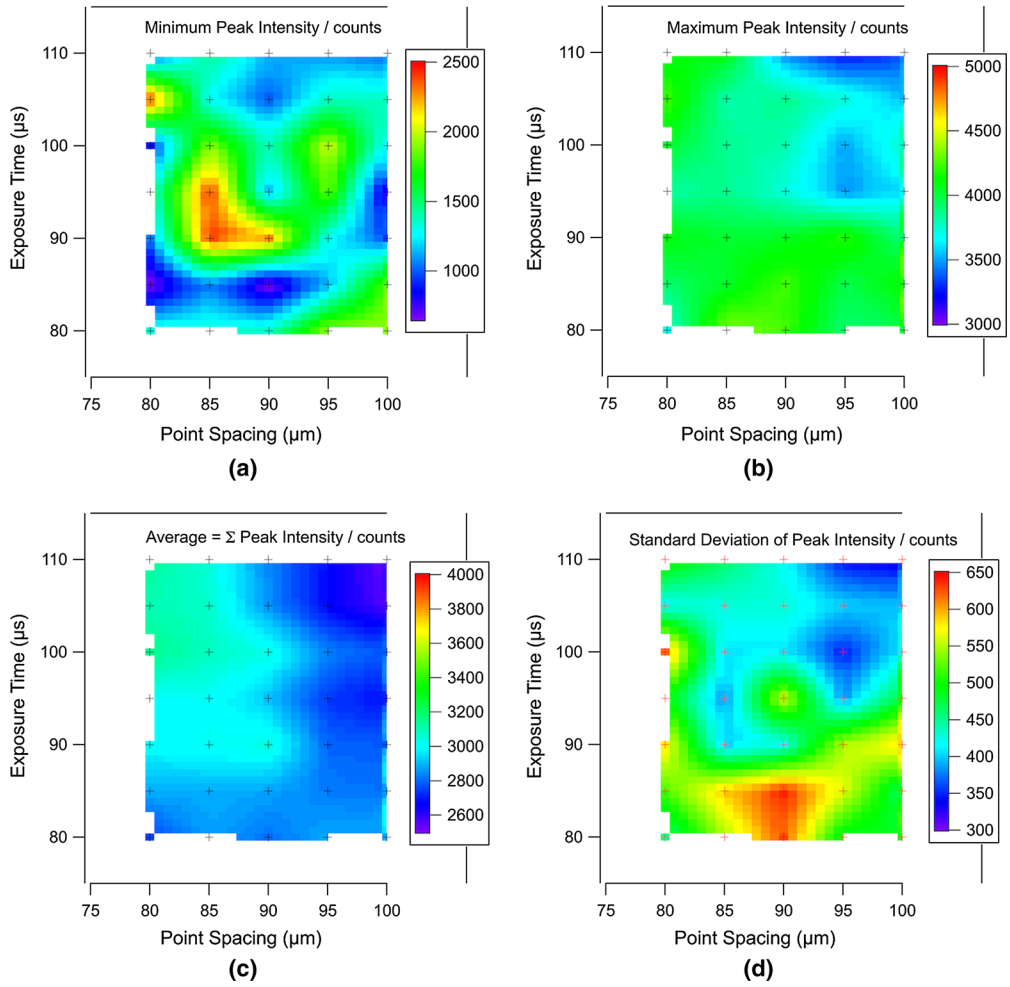

Fig. 5—Statistical analyses of all the IR thermal signatures as a function of point spacing and exposure times: (*a*) minimum; (*b*) maximum; (*c*) average; and (*d*) standard deviation.

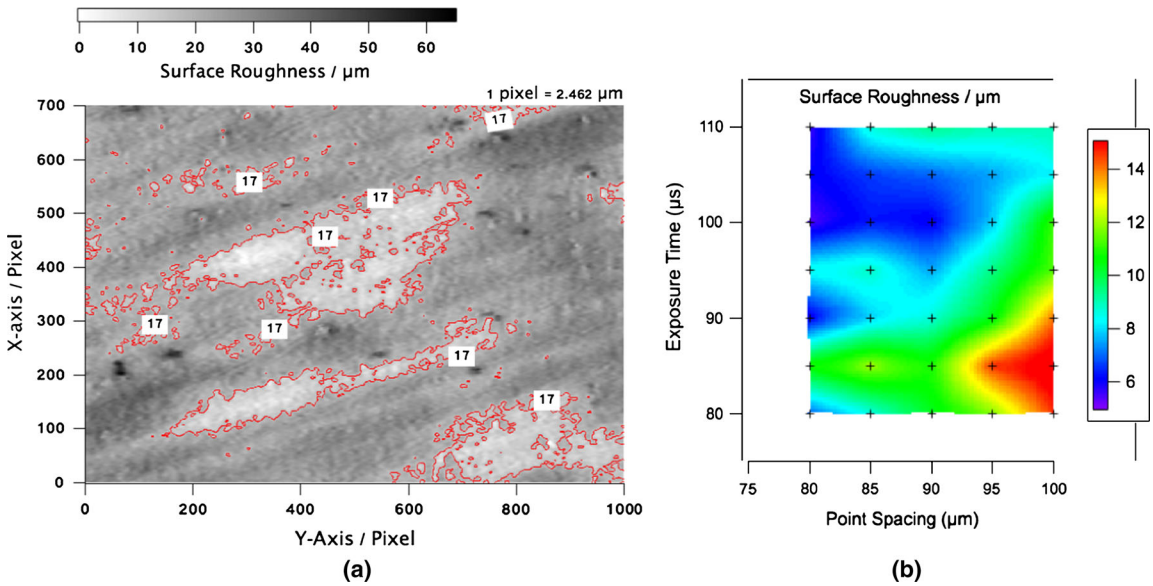

Fig. 6—(*a*) Typical surface roughness data from the surface of a cube showing the presence of plateau- or mesa-like features that connect one or more beads; (*b*) overview of the average surface roughness data for all of the top surfaces of the cubes as a function of processing conditions.

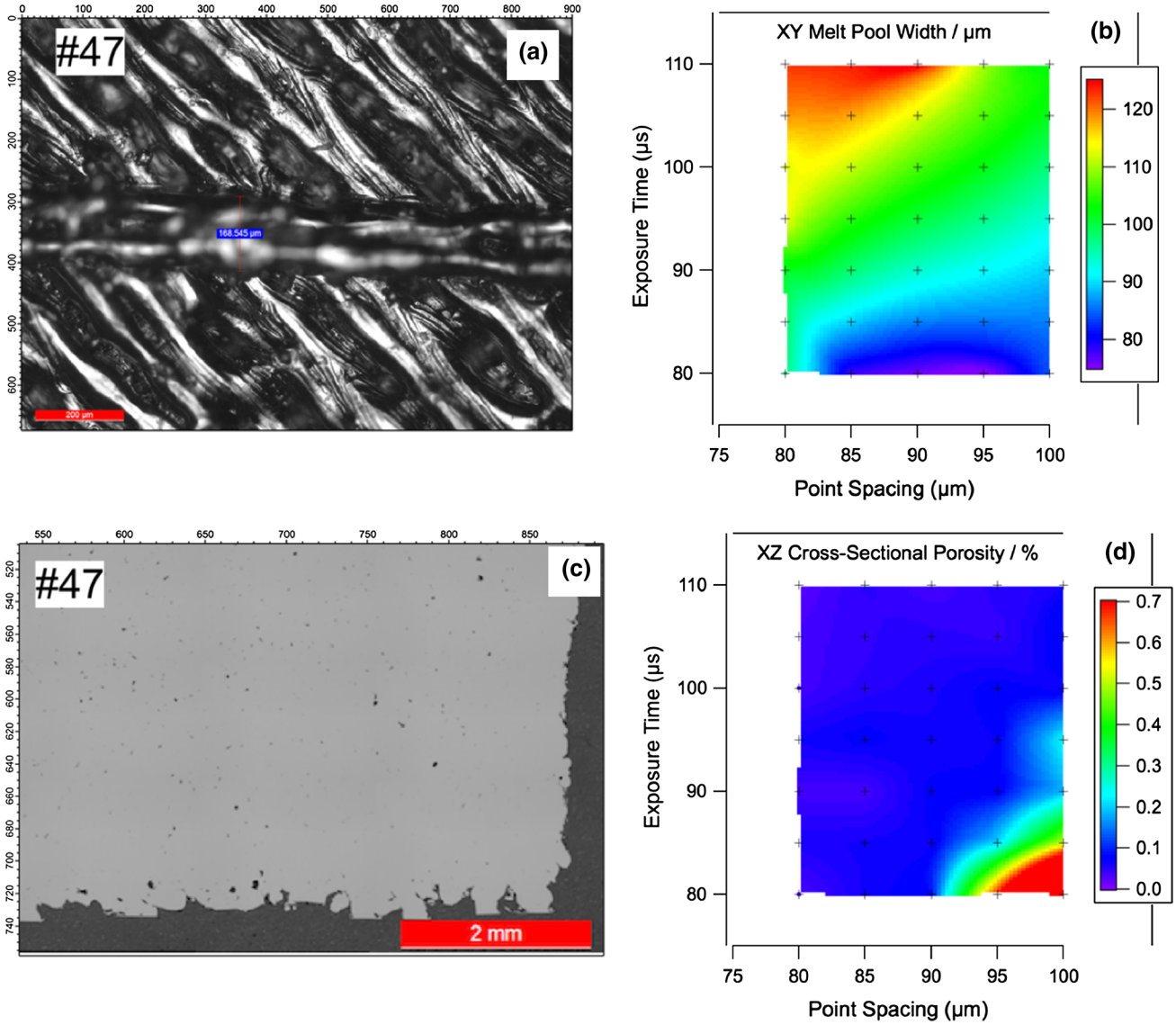

Fig. 7—Overview of the melt surface patterns (*a*) on the XY surface, (*b*) the average variations of melt pool widths are compared with, (*c*) a tendency to form porosity at different locations in the XZ sections, and (*d*) the average variations of cross-sectional porosity as a function of processing conditions.

Our comprehensive data are indeed quite relevant to these current research directions; however, it is necessary to discuss the generality of the current results with reference to complex thermal conditions typical to that of the L-PBF process.

A. *Correlation of IR Peak Intensity with Build Failure*

Detailed analyses of all IR video files from the top layer resulted in interesting observations with reference to maximum intensity. The intensity decreased gently as the process parameters moved to less ideal conditions with higher degrees of defect formation, as well as, large increases in intensity when the builds failed due to uncontrollable swelling and excessive spatter (Figures 3 and 4). Since the exact conversion of the IR data to temperatures was not deemed consequential for the purposes of this study, one may assume that the peak IR intensities are related to area within the melt pools that were heated above the evaporation temperature creating a bright plasma.[36,37] Therefore, one may be able to correlate the observed IR brightness to the localized melting conditions. To calculate the area under the laser beam that may experience different temperature distributions, analytical equations developed for welding were leveraged [38] (see Appendix A2). Typical temperature distributions, assuming the two different thermal conductivities corresponding to nickel powders ($k_{\text{powder}} = 0.15\ k_{\text{solid}}$) and solid nickel ($k_{\text{solid}} = k_{\text{bulk-nickel}}$) are shown in Figures 13(a) and (b), respectively. As expected, when the melting occurs on top of the powder bed with no solid underneath, the area of the melt pool that is above the evaporation (3190 K) temperature is higher than for conditions of melting powder on top of the solid material. In the next step, the evaporated area was calculated for all of the conditions

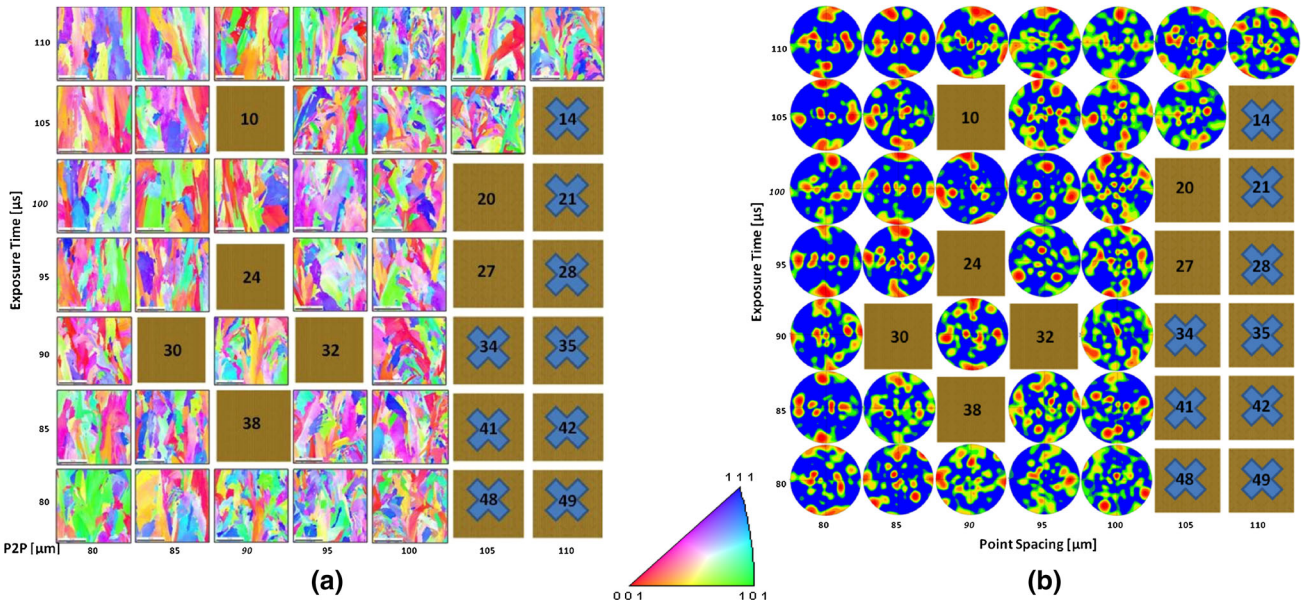

Fig. 8—Overview of the solidification microstructure as a function of processing conditions: (*a*) inverse pole figure (IPF) misorientation maps and (*b*) pole figures for the same conditions. The data show a gradual change in columnar solidification mode to misoriented growth mode with an increase in point spacing and reduction in exposure time.

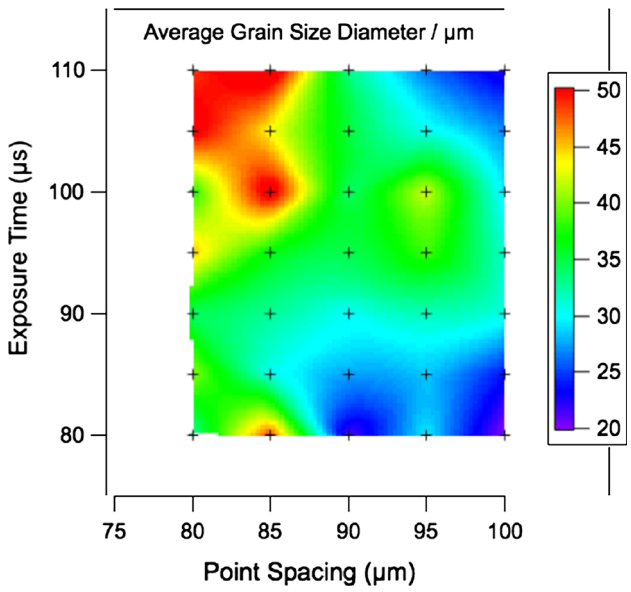

Fig. 9—The measured average size of highly misoriented FCC grains as a function of point spacing and exposure time.

(effective laser scan velocity) and was compared with the measured IR peak intensity. Interestingly, the evaporated area for sound components and poor components lies on two different extrema and correlates with two different extrema measured for bulk melting and failed build conditions (Figure 13(c)). This analysis confirmed that the measured IR intensity can be correlated to the general reduction in build quality with an increase in point spacing. Furthermore, drastic changes in build quality related to delamination effects were observed with poor choices of point spacing. Based on these results, we recommend that the IR intensity be measured, as a function of location, while building complex geometries for long runs which may be referred to for diagnoses of build failure problems.

B. *Rationalization of Build Quality with Process Parameters*

1. *Surface roughness*

The better average surface roughness measurements can be rationalized further by looking at a schematic representing the melt pool overlaps (Figure 14). Intuitively, it is expected that closer point spacing, or hatch spacing, leads to more melt pool passes per layer, which in turn would lead to more overlap and thus an overall smoother surface finish (Figure 14(a)). Increasing point spacing would then lead to more hill-and-valley type effects (Figure 14(b)), which in turn, would change the powder packing distribution, with powder particles filling more of the valleys than the hilltop areas, and as such, the proceeding layer melting would not be capable of compensating for the surface roughness. Schematic illustrations of problems associated with inferior overlap, due to changes in point spacing and limited amount of melting, are shown in Figure 14(c). As a result, this compounding effect of insufficient point spacing induces additional layer height variations which may manifest itself in the subsequent layers that continue to propagate through the height of the build. If our hypothesis is indeed correct, we should see consistent increases in the frequency distributions of the surface roughness for the top layer as a function of the increase in point spacing and also the decrease in exposure time. Summary of statistical analyses for all of the roughness data from the top surfaces is compared in Figure 15. As expected, the surface roughness distributions increased, suggesting that with a reduction in

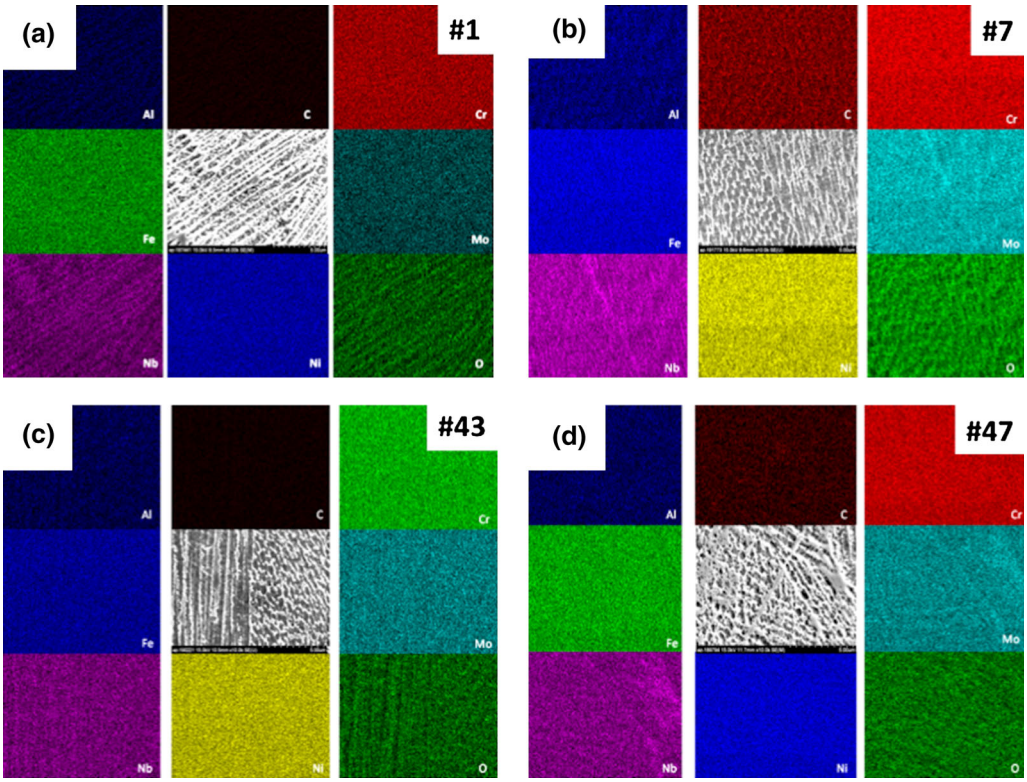

Fig. 10—Overview of energy-dispersive X-ray maps (Al, C, Cr, Fe, Mo, Nb, Ni, and O) from selected, variable extreme, cube sample conditions showing the dendritic microstructure and strong partitioning of Nb, as well as some tentative association of oxygen enrichment near the interdendritic regions. (*a*) sample #1; (*b*) sample #7; (*c*) sample #43; and (*d*) sample #47.

melting and melt bridging across points and hatches, one would expect increased tendencies for build failure and defect generation.

2. *Build quality*

Researchers from Carnegie Mellon University[39–41] have developed processing maps based on simple analytical heat transfer equations that are based on classic Rosenthal equations.[42] This model allows for the estimation of single-track melt pool width and depth. Therefore, in this section, correlations between predicted single-track melt pool geometry and measured build characteristics including melt pool width, melt pool depth, surface roughness, and porosity were attempted using the Rosenthal equation. The heat transfer equations shown in Appendix A2 were calibrated by varying the efficiency parameter (η) until the predicted melt pool widths compared with the measured widths as a function of laser scan velocity. The measured melt pool widths can be correlated within a band of predictions made with efficiency parameters varying from 0.1 to 0.2 (Figure 16(a)). This low value of energy efficiency is also reported by laser welding with low powers in the range of 200 W.[43] With the same analyses, the melt pool depths also can be calculated (Figure 16(b)). The predicted melt pool depths were also compared with the measured surface roughness. It is interesting that when the predicted melt pool depths are similar or above the powder layer thickness, the surface roughness also reduces to the same order of magnitude as the powder layer thickness. Under these conditions, one may expect good builds with minimal lack of fusion defects. Therefore, the measured porosity was also compared for the same conditions (Figure 16(c)). The correlations show that as soon as the measured surface roughness falls below 20 to 40 μm, the porosity also drops below 0.1 pct.

Based on the above analyses, it appears that semi-empirical correlations arrive at optimum build conditions, *i.e.*, if the predicted melt pool widths are greater than the point spacings, and melt pool depths are greater than layer thickness, the build quality is expected to be robust.

C. *Rationalization of Solidification Microstructure*

1. *Solute partitioning during solidification*

The EDS maps showed the tendency for the segregation of varying alloying elements to the boundaries between fine primary dendrite arms. This phenomenon is not new and is often observed in microstructures within weld metal regions and in E-PBF and DED processes. Interestingly, the SEM micrographs show pronounced segregation of Nb, Mo, and O compared to other elements. Although, one can dismiss these apparent differences (especially carbon) based on the sensitivity of the SEM-EDS analysis methodologies, we evaluated the possibility of trapping these elements due to rapid liquid–solid interface velocity (R). Aziz[44] derived a fundamental equation to evaluate the tendency for velocity-dependent partitioning (k_v^i) as a function of liquid–solid interface velocity ($R_{L/S}$), which is given below.

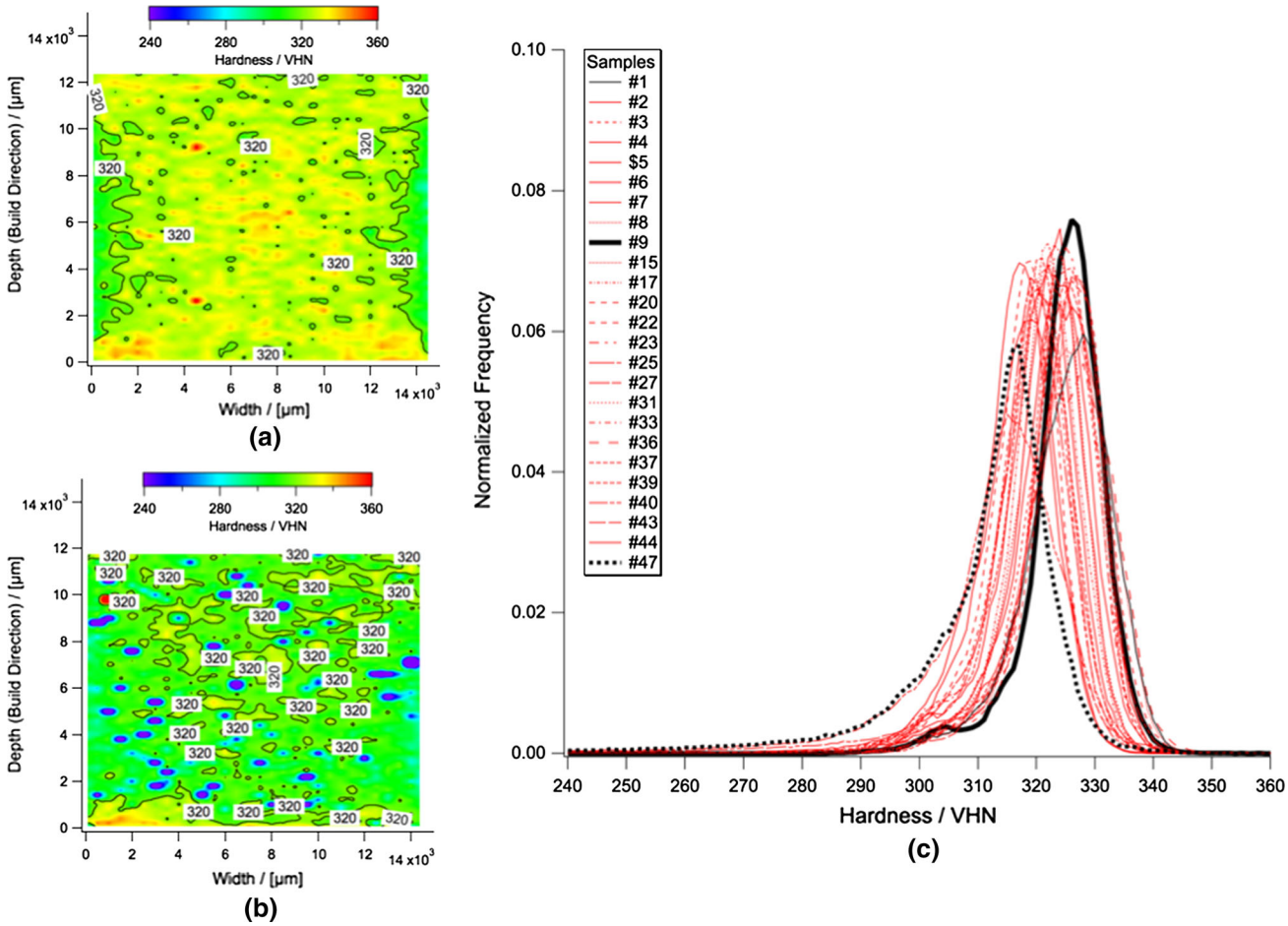

Fig. 11—Hardness maps collected along the XZ cross sections of (*a*) sample #9 and (*b*) sample #47 showing the spatial distribution of hardness. (*c*) The summary histograms plotted for all of the data from other samples compared with that of samples #9 and #47.

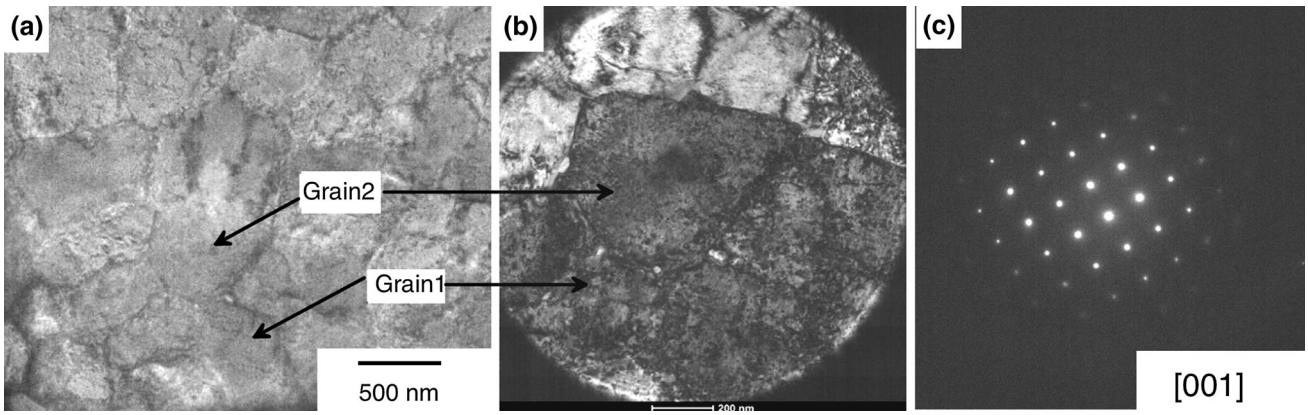

Fig. 12—Summary of transmission electron microscopy images from the sample #12: (*a*) fine cellular structure at low magnification and (*b*) high magnification image showing excessive dislocation density. (*c*) Electron diffraction information confirmed no evidence of 2nd phase precipitation including γ' and γ'' phases.

$$k_v^i = \frac{k_0^i + a_0\left(R_{\mathrm{L/S}}/D_i\right)}{1 + a_0\left(R_{\mathrm{L/S}}/D_i\right)}. \qquad [3]$$

In the above equation, k_0^i is the equilibrium partitioning coefficient for the ith element in the alloy, D_i is the diffusivity of the same element along the L/S boundary, and a_0 is the characteristic diffusion distance, which is assumed to be 3 Å. The equilibrium partitioning ratios for all elements are calculated using ThermoCalc® software with TCNi8 database. The above equation was used to calculate the conditions that may

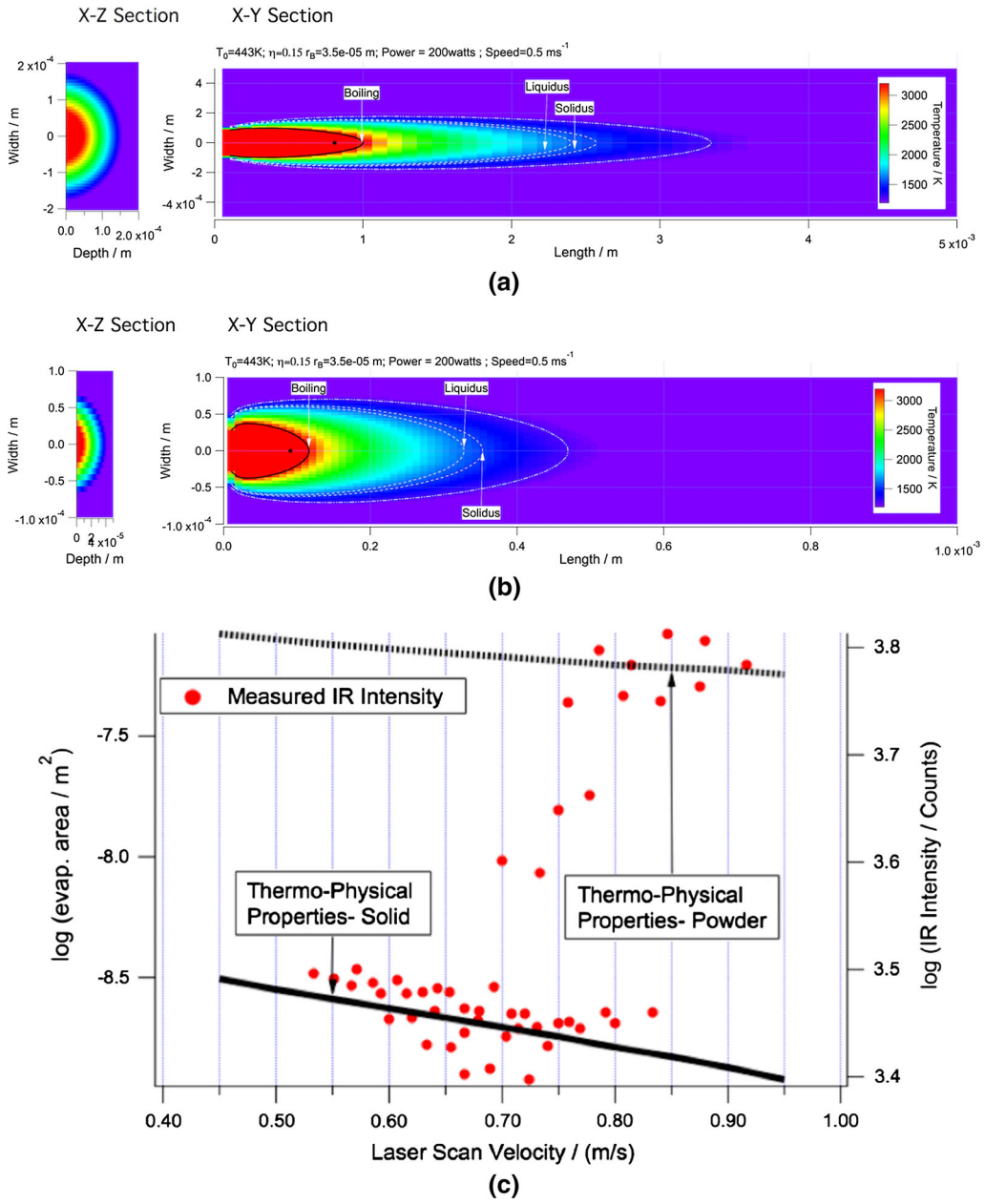

Fig. 13—Calculated temperature distribution using the analytical model for two different thermal conductivity conditions: (*a*) low thermal conductivity representative of melting on a powder bed; (*b*) high thermal conductivity representing melting upon solid IN718. All other parameters are kept constant: laser powder = 200 W; preheat = 443 K; efficiency = 15 pct; radius of laser beam = 35 μm and speed of 0.5 m/s. (*c*) Empirical correlation of the region above the boiling point with IR intensity.

lead to solute trapping, assuming the same diffusivity (5×10^{-9} m^2/s) values for all elements.[45] Note that the experimentally measured diffusivity of alloying elements in complex alloy systems is very rare[46] and therefore, these values should not be considered as accurate.

The calculations were also performed with reducing and increasing the diffusivity by one order of magnitude at a time. As expected, with the reduction in diffusivity, the conditions for solute trapping were found to move to lower velocities and *vice versa* for conditions with increased diffusivity. Based on these calculations (Figure 17(a)), it is indeed clear that the conditions for solute partitioning to the interdendritic regions for Al, Fe, Cr, and Co are expected to be minimal, while the partitioning of Mo, Nb, O, and C to the interdendritic regions would be favored, even with very high liquid–solid interface velocities (*e.g.*, 10 m/s). The next point is to understand the interdendritic microstructure that could form during final stages of solidification due to preferential enrichment of Mo, Nb, O, and C. To answer this question, we performed Scheil solidification simulations with ThermoCalc® software.[47] As

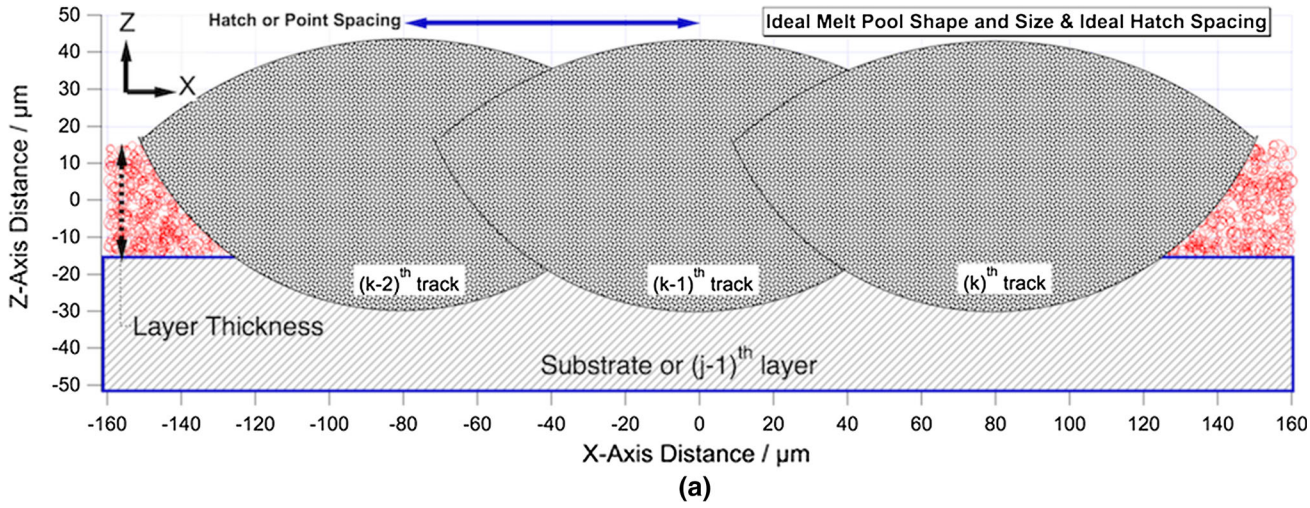

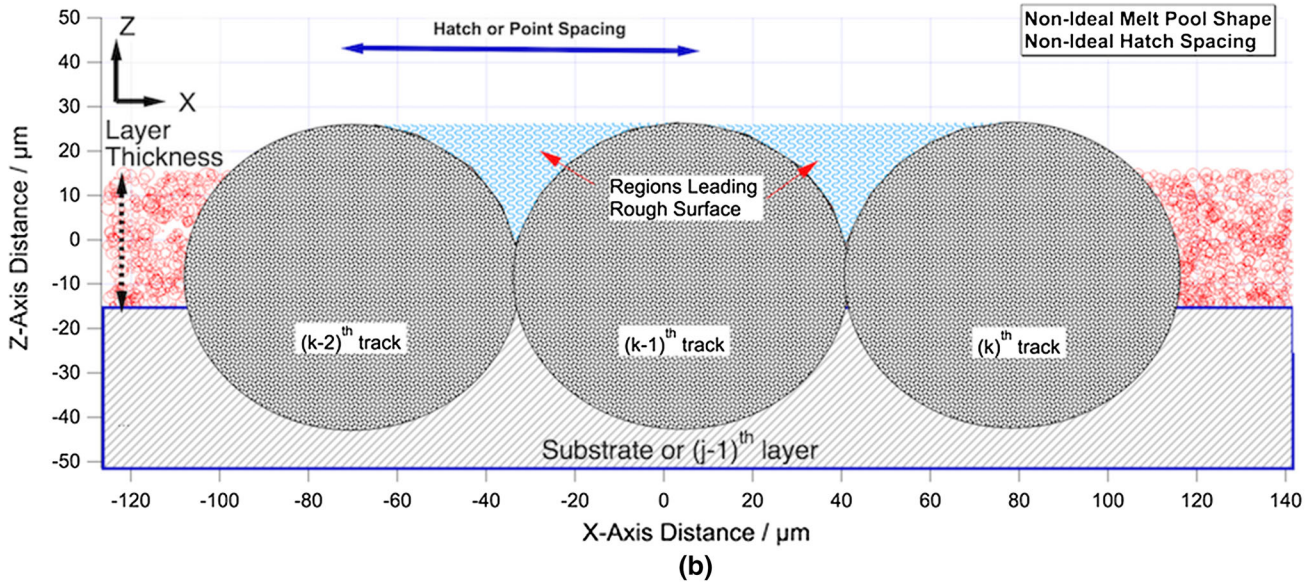

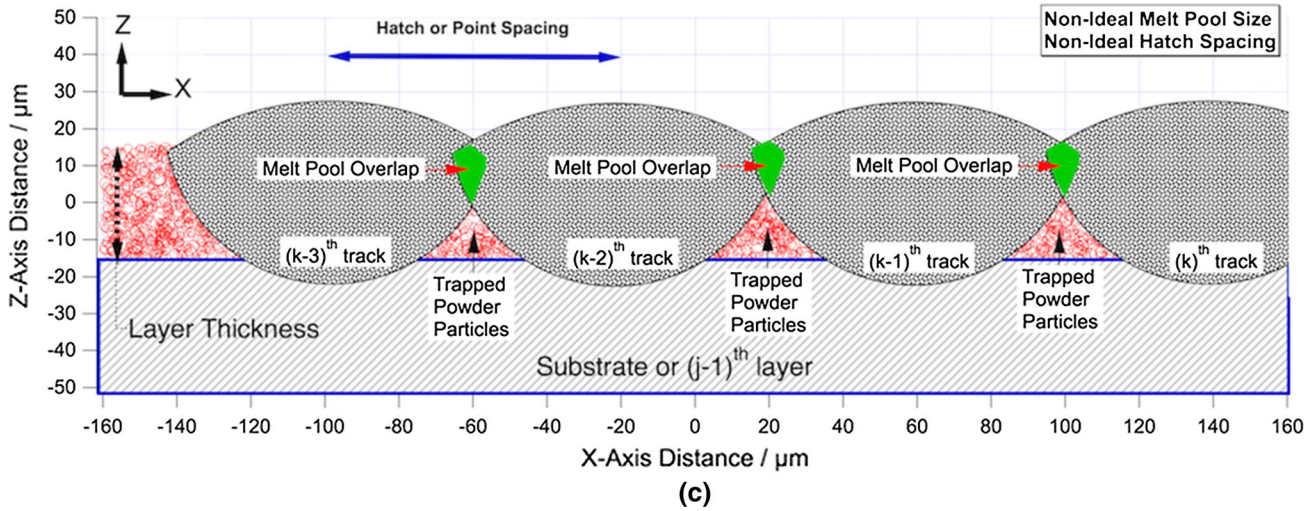

Fig. 14—Schematic illustration of the mechanisms for smooth surface finish (*a*) due to the close overlap of the molten beads and (*b*) rough surfaces due to the large separations between molten beads. (*c*) Schematic of the mechanisms for the formation of porosity due to the lack of fusion of previously deposited melt beads.

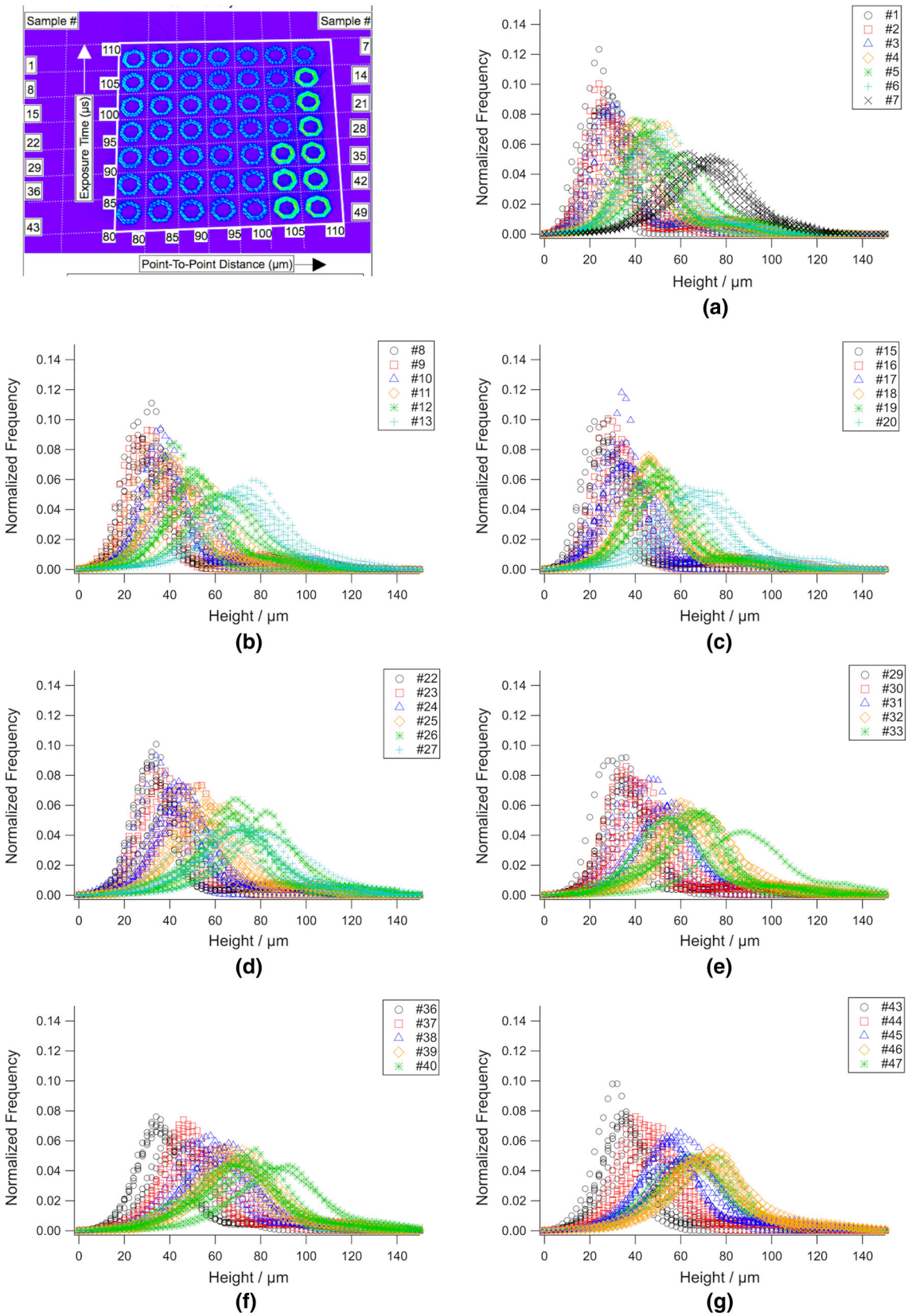

Fig. 15—Summary of the surface roughness data for all cube samples showing gradual increase in roughness with an increase in point spacing and reduction in exposure time. The image on the top left shows the sample identifications and their processing conditions. Surface roughness data from different sets of samples are provided above: (*a*) #1 to #7; (*b*) #8 to #13; (*c*) #15 to #20; (*d*) #22 to #27; (*e*) #29 to #33; (*f*) #36 to #40; and (*g*) #43 to #47.

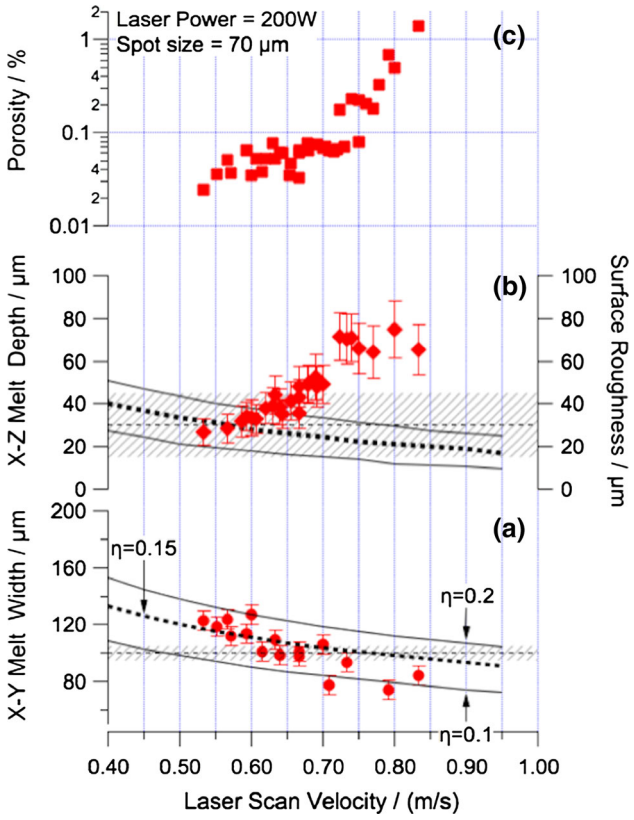

Fig. 16—Correlation of calculated (*a*) melt pool width and (*b*) depth with surface roughness and (*c*) lack of fusion porosity. The grayed region in (a) corresponds to the point spacing of 90 μm and in (b) corresponds to layer thickness with spread dictated by the powder size distributions.

expected, with the progression of solidification, the calculations (Figure 17(b)) predicted the onset of the following interdendritic phases, MX, Ni_3Nb, Laves, σ, and corundum. None of our SEM or TEM characterization results were able to identify these phases due to the sample preparation techniques, limited spatial resolution, and the field of view of the samples. Future work is necessary to identify these precipitates with focused ion beam techniques.

2. *Primary dendrite arm spacing*

The uniqueness in the current solidification microstructure, with reference to results from Inconel® 718 builds made by other additive manufacturing processes, is related to the length scale over which these segregations occur in-between the primary dendrite arm spacing. Quick evaluation of the micrographs from Figure 10 showed that the primary dendrite arm spacing was on the order of 0.45 ± 0.1 μm. The primary dendrite arm spacing for Inconel® 718 alloy under E-PBF conditions was measured to be around 12 μm. These differences are rationalized by using fundamental equations relating the primary dendrite arm spacing (λ, μm) with G and R, given below.

$$\lambda = C/G^{0.5}R^{0.25}. \quad [4]$$

In this equation, C is a proportionality constant that may take the values from 2145.952 to 3195.214, G is thermal gradient (K/m), and R is the liquid–solid interface velocity (m/s). Using Eq. [4] and the measured primary dendrite arm spacing, the bounding values for

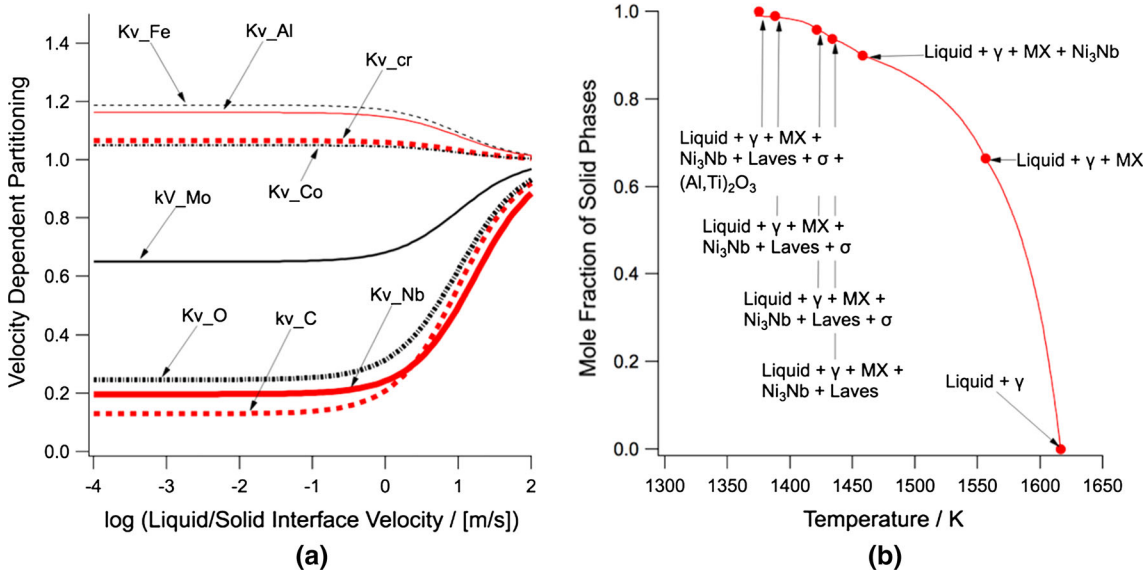

Fig. 17—Calculated tendency for (*a*) non-equilibrium partitioning of alloying elements as a function of liquid–solid interface velocity and (*b*) Scheil–Gulliver solidification simulation based purely on thermodynamics.

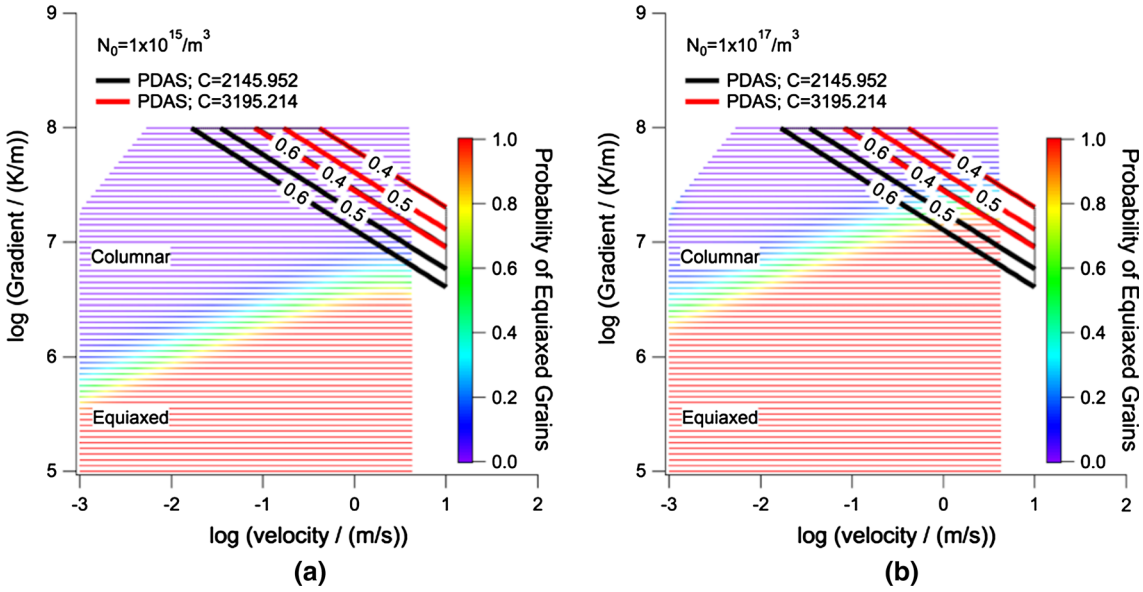

Fig. 18—Estimated ranges of G and R from the measured primary dendrite arm spacing bounding box are overlaid with the calculated solidification maps, with two different initial number densities of nuclei ahead of the L/S interface: (*a*) $N_0 = 10^{15}$ m^{-3} and (*b*) $N_0 = 10^{17}$ m^{-3}.

Table II. Thermal Simulations Conducted Using the Gleeble® 1500D and Resulting Hardness Measurement Results

Sample	Thermal Simulation	Average Hardness, VHN	Range, VHN
Cube #12	as-built condition	324	309 to 340
G1	heating rate of 10 °C/s up to 1050 °C & 5s hold at 1050 °C & cool at 1 °C/s cooling to 25 °C	303	285 to 325
G2	heating rate of 10 °C/s up to 1050 °C & 5s hold at 1050 °C, 5 °C/s cooling to 25 °C	288	270 to 309
G3	heating rate of 1050 °C/s up to 1050 °C & 2s hold at 1050 °C, 1 °C/s cooling to 25 °C	291	273 to 308
G4	heating rate of 1050 °C/s up to 1050 °C & 2s hold at 1050 °C, 5 °C/s cooling to 25 °C	285	229 to 302
G5	heating rate of 1.5 °C/s up to 877 °C & 1.5 °C/s cooling to 25 °C	348	315 to 371
G6	heating rate of 1 °C/s up to 877 °C & 1 °C/s cooling to 25 °C	350	329 to 364
G7	heating rate of 0.1 °C/s up to 877 °C & 0.1 °C/s cooling to 25 °C	371	347 to 388
G8	heating rate of 0.01 °C/s up to 877 °C & 0.01 °C/s cooling to 25 °C	395	320 to 413

operational *G* and *R* values during L-PBF were derived. The bounding box was calculated using the two "*C*" values that resulted in the following limits: {*G* (K/m), *R* (m/s)} = {10^8, 0.01758} {10^8, 0.4078}, {2.2022×10^7, 10}, and {4.0476×10^6, 10}. Since we cannot correlate the observed microstructure location to the spatial-temporal measurements of *G* and *R*, we need to understand the validity of the above estimations based on the solidification grain texture.

3. *Crystallographic texture*

The analyses of the data in Figure 8 showed transitions from highly textured columnar grain structure to randomly misoriented grain structure. In the literature, the tendencies for such drastic changes in the solidification texture have been correlated to spatial and temporal variations of thermal gradients (*G*) and liquid–solid interface velocities (*R*). Careful analyses showed that the misoriented growth appeared to occur with an increase in point spacing and decrease in exposure time. Both of these conditions are expected to reduce the superheat of the liquid metal and the melt pool shape, as well as increase the L/S interface velocity. Since we have estimated the bounding values for *G* and *R* based on the primary dendrite arm spacing, the CET transitions were calculated using interface response function theories.[45,48] Details of these calculations have been provided in the Appendice. The calculations (see Figure 18) show that for the range of *G* and *R* values, if we assume low number (1×10^{15} m^{-3}) of pre-existing nuclei (N_0) ahead of the L/S interface, the CET transition may not occur. However, if the N_0 value is increased by two orders of magnitude (1×10^{17} m^{-3}), the probability of CET increases. Currently, there are no experimental methods to measure the N_0 value under *in situ* conditions. However, based on the welding[49] and laser

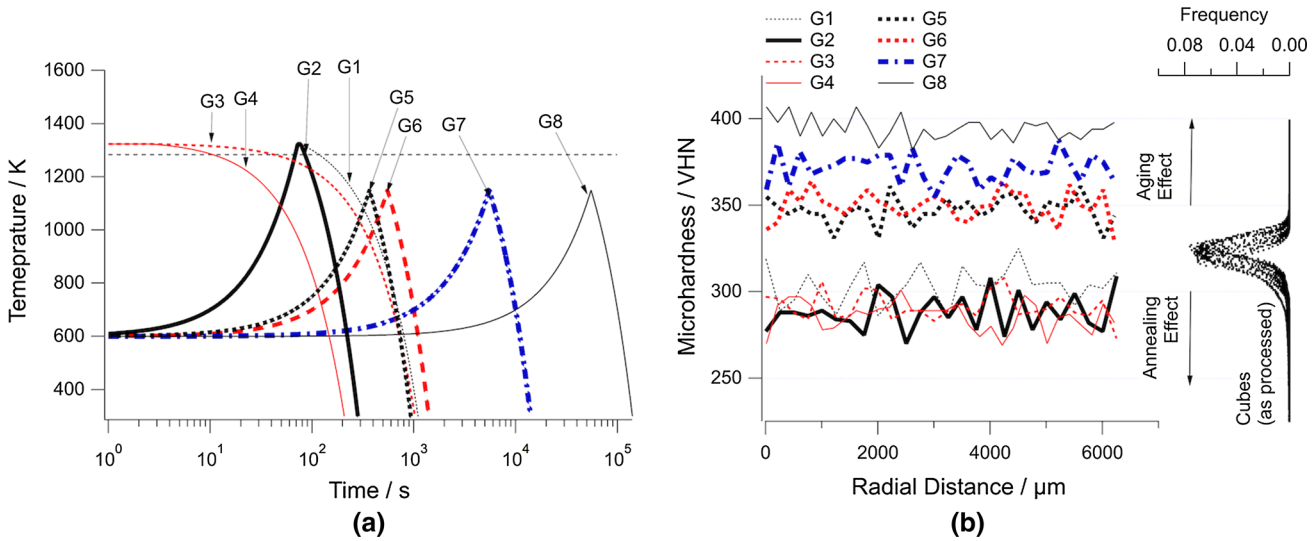

Fig. 19—Post-processed Gleeble® thermal cycling (Table II) performed to evaluate the annealing and aging effects: (*a*) thermal cycles; (*b*) hardness maps across the radial direction from the center of the Gleeble® samples. The hardness histograms from the as-built condition are also shown to emphasize the annealing and aging effects.

surface alloying literature,[50,51] one can state that with a reduction in the superheat of the liquid metal, the melt pool shape may retain many of the unmelted powders, potentially acting as heterogeneous nucleation site. The role of non-dissolving oxides, carbides, nitrides on the breakdown of columnar grain solidification has been shown in welding,[52] laser surface alloying, and L-PBF processes. For example, the recent work by HRL,[53] on the addition of functionalized powders to initiate equiaxed nucleation, can also be rationalized based on the above knowledge. Based on the above discussions, it appears that the theories of welding metallurgy can be extended to rationalize the solidification microstructure in the L-PBF builds that are seen in the as-deposited conditions.

D. *Rationalization of Hardness Heterogeneity and Solid-State Transformations*

Earlier, the heterogeneity observed in the hardness maps was attributed to the accumulated plastic strains that occur during transient thermal stress evolution during processing. This phenomenon and associated residual stresses are well known in welded structures,[54–56] as well as confirmed in additive manufacturing,[57,58] but the stability of the accumulated plastic strains has to be confirmed *via* post-process heat treatment characterization. To accomplish this, standard samples for Gleeble® thermal-mechanical simulations were fabricated using the processing conditions of Cube #12. Then, these samples were subjected to thermal simulations (Table II), shown in Figure 19(a), using a Gleeble® 1500D simulator. Samples G1 through G4 represented thermal annealing conditions, while G5 through G8 were used to evaluate the possibility of inducing specific precipitations by aging. Hardness tests were performed on all of the simulated samples, and

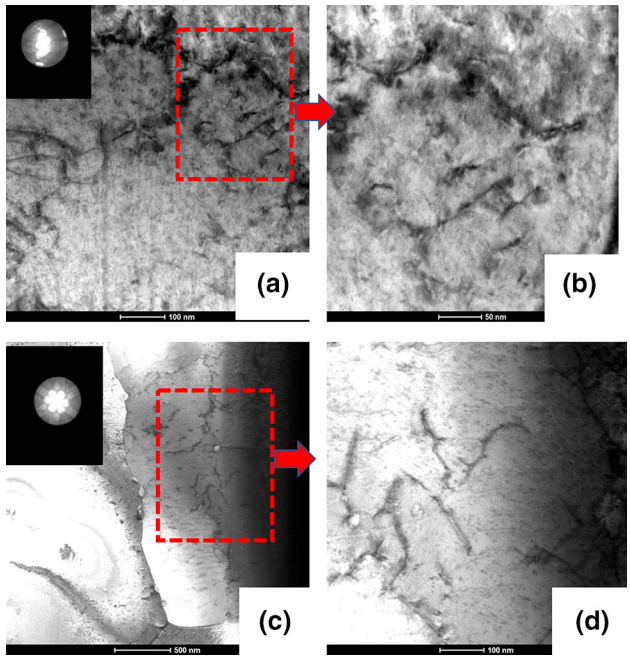

Fig. 20—Transmission electron microscopy of (*a*, *b*) G1 and (*c*, *d*) G2 samples confirming the reduction of the original dislocation density, while selected area diffraction patterns confirmed the absence of the age-hardening precipitates.

because of the uncertainty of the build direction after machining of the Gleeble® parts, hardness measurements were conducted across four lines, rotating 45 deg and traversing the diameter each time over the cross-sectional area (Figure 19(b)).

The data clearly showed that thermal annealing treatments (G1 to G4) softened the builds and the aging thermal cycles (G5 to G8) hardened the build

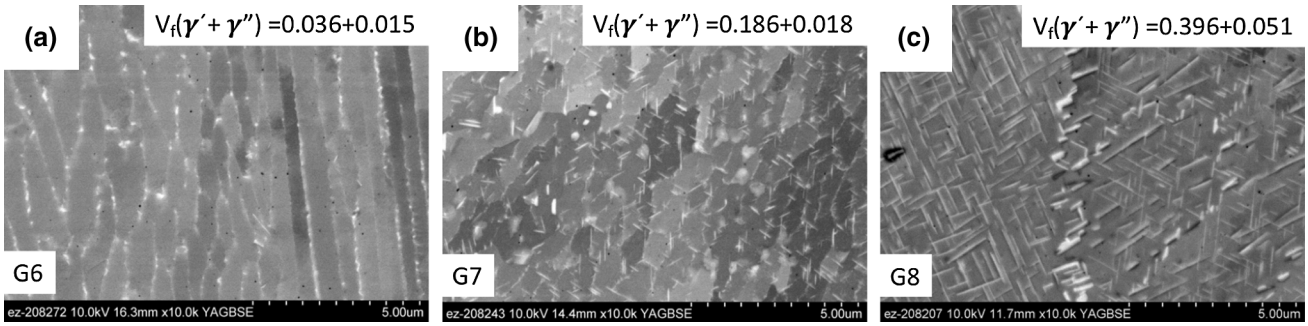

Fig. 21—Scanning electron microscopy images from samples subjected to different thermal cycling: (*a*) G6, (*b*) G7, and (*c*) G8. The volume fraction for each of the conditions was also measured using image analysis and are provided with each image.

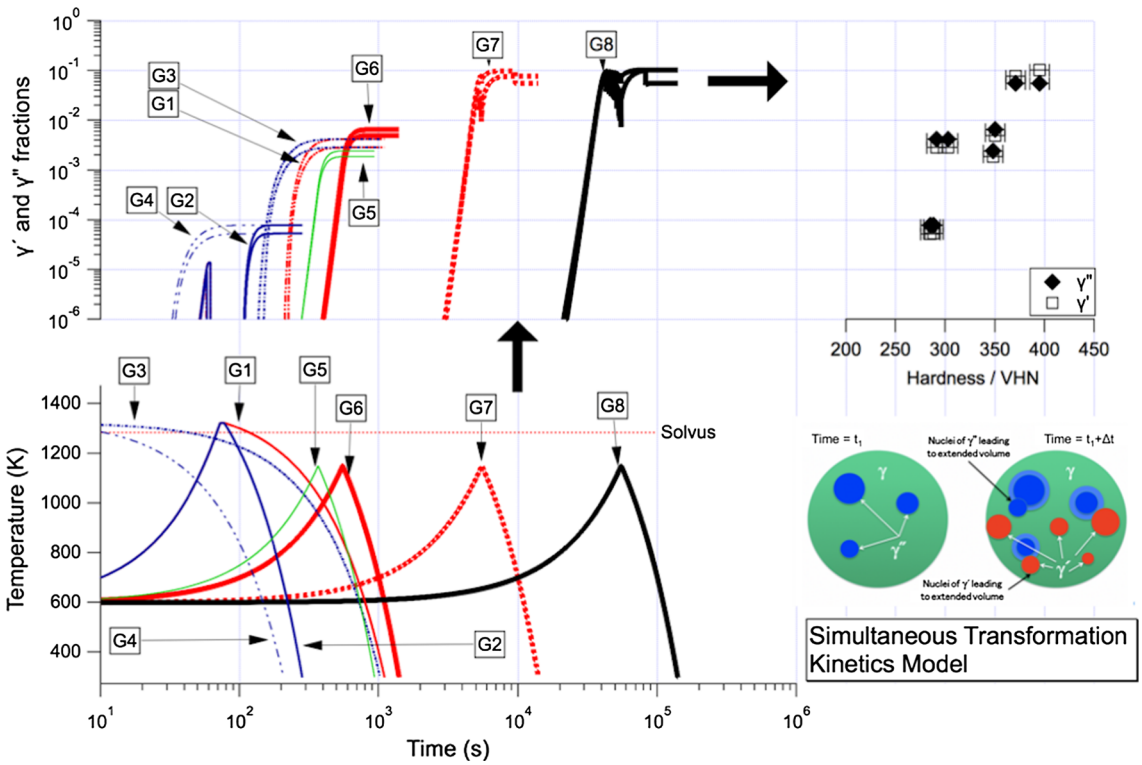

Fig. 22—Overview of the calculated phase fractions of γ' and γ'' as a function of thermal cycles, using the STK model; bottom: thermal cycles; top left: the corresponding evolution of the precipitate fractions; top right: correlation of the predicted volume fractions of age-hardening precipitates and the average hardness.

samples, with reference to the as-processed condition. To confirm that the softening was attributed to the reduction of the dislocation density, transmission electron microscopy analyses (Figure 20) were performed on G1 and G2 samples. The imaging conditions were set at slightly off from [001] zone axis to allow for imaging of dislocations. The analyses qualitatively confirmed that there was a distinct reduction in the dislocation density. To confirm precipitation during the aging treatments in a quantitative way, only G6, G7, and G8 samples were characterized in detail using scanning electron microscopy (see Figure 21).

The samples were imaged in the as-polished condition using backscattered imaging. With this mode, the Nb-rich precipitates would appear brighter in contrast, but since SEM cannot distinguish the nanoscale co-precipitation of γ' and γ'' precipitates, the precipitates were quantified as aggregates. Initially, the precipitation appears to be enhanced close to the interdendritic regions (G6) and then spreads to the interior of the grains (G8). This was indeed expected and can be correlated to the solute segregation described earlier. In the next step, the published STK model[59,60] was used to evaluate the extent of precipitation for all of the G1 to G8 thermal cycles. The calculated volume fractions of γ'

and γ'' precipitates (see Figure 21) correlated well with the measured hardness values (Figure 22).

V. RELEVANCE TO AM AND CHALLENGES

Our original intent of this research was to develop a comprehensive, extensible data set and analytical tools to allow AM practicing engineers to understand the overall process flow and its effects on defect, microstructure, and property evolutions. As discussed above, we have developed correlations between data measured by *in situ* and *ex situ* characterization techniques with phenomenological models, but we believe there are many unanswered questions that need to be addressed with the continuing refinement of our analytical tools. These questions are outlined briefly here. (i) *Uncertainty of IR measurements* as discussed by Raplee *et al.*[31] the IR measurements are affected by the curvature of the surface and also by the emissivity changes as the powder state transitions to liquid and then to solid. Therefore, we need additional *in situ* tools to track the variations of the surface conditions under *in situ* conditions. (ii) *Evaluation of sub-surface defects* Although IR images are very good at providing qualitative information about the possibility of defect formation, it does not provide any information about the sub-surface defect formation or annihilation. (iii) *Time and spatial resolution* The current spatial and temporal resolutions are not on the same order of the phenomena that controls the solidification and solid-state transformations. Incorporation of high-end IR cameras, data recording storage devices, and analytical tools may turn out to be more expensive than that of the L-PBF machines themselves, thereby limiting the use of these methods. Therefore, we need to develop hybrid techniques that are capable of using less expensive IR equipment and surface sensors, combined with the use of fast-acting analytical models to interpolate the thermal and mechanical conditions to finer time and spatial resolutions. (iv) *Ability to measure plastic deformation* Current results have shown that processing conditions lead to local thermal stresses that may result in accumulated plastic strains lingering in the as-processed state of the final components manufactured *via* AM; however, none of the current *in situ* characterizations was capable of detecting these changes under *in situ* conditions. Future work must focus on indirect methods to extract this information. (v) *Data Analytical tools* Although, we have developed ad hoc analytical tools using existing software infrastructures, more work is necessary to package these analytical tools into an integrated package.

VI. CONCLUSIONS

This work has demonstrated pathways to employ *in situ* and *ex situ* characterization techniques with pragmatic uses of existing welding analytical models to describe defect formation, solidification, and solid-state phase transformations during the laser powder bed fusion of Inconel® 718. Because of these determined connections, the following specific conclusions could be made. (i) The *in situ* IR imaging and analyses of integrated intensities can provide qualitative evidence for the robustness of the L-PBF process in terms of the melt pool characteristics and potential tendency for build failures. (ii) Based on the combination of *in situ* IR data, *ex situ* surface roughness measurements, macrostructure characterizations, and calibrated welding heat transfer models, a simple design rule for avoiding the lack of fusion defects and porosity has been proposed. (iii) It is possible to estimate the prevailing spatial and temporal variations of the thermal gradient and the liquid–solid interface velocity during L-PBF process through measurement of the primary dendrite arm spacing. (iv) Calibrated columnar to equiaxed solidification maps, based on interface response function theories, are able to provide rationalization of the observed solidification texture variations as a function of laser exposure time and point spacing. (v) The observed solute partitioning of niobium was rationalized based on the Scheil solidification model, and furthermore, the solidification conditions in the current experiments did not reach the solute trapping conditions. (vi) The Gleeble® thermal cycling experiments, electron microscopy, and simultaneous phase transformation kinetic (STK) models rationalized the microstructural pathway involving accumulation of plastic deformation and no precipitation in the as-processed conditions, reduction of dislocation density and softening on heat treatment above the solvus temperature, and copious precipitation on slow heating and cooling below the solvus temperature.

ACKNOWLEDGMENTS

The authors of this work would like to acknowledge and thank the funding contributor Applied Optimization, Inc. under the NASA STTR Phase II program (Contract Number: NNX15CA24C). Part of the research is based upon work supported by the US Department of Energy, Office of Energy, Efficiency, and Renewable Energy, Advanced Manufacturing Office under Contract Number DE-AC05-00OR22725. The microscopy was supported by using instrumentation (FEI Talos F200X S/TEM) provided by the Department of Energy, Office of Nuclear Energy, Fuel Cycle R&D Program and the Nuclear Science User Facilities. D.W. Coffey assisted with the experimental work. The United States Government retains and the publisher, by accepting the article for publication, acknowledges that the United States Government retains a non-exclusive, paid-up, irrevocable, worldwide license to publish or reproduce the published form of this manuscript, or allow others to do so, for United States Government purposes. The Department of Energy will provide public access to these results of federally sponsored research in accordance with the DOE Public Access Plan. (http://energy.gov/downloads/doe-public-access-plan).

APPENDICES

Appendix A1: Hardware Setup for In Situ Infrared Imaging

The details of our IR imaging experiments, installed within the Renishaw® AM250 machine, are briefly summarized. The geometry of the IR camera placement is shown in Figure A1. A front surface mirror was positioned inside the build chamber to allow for the camera to access the whole field of view available for the AM processing surface. Due to the use of the mirror at a certain angle, we did have keystone distortions in the image. Although, we can correct the images using matrix methods, this was not done to avoid any interpolation effects. The IR camera was equipped with a 25mm germanium lens with a neutral density #2 filter. A 1TB solid-state high-speed data recorder was used in order to take images at high speed for the entire layer collection. Custom-built programs were written using MatLab® and IgorPro® software packages to extract the IR intensity, as well as, to do visualization and statistical analysis.

All the recorded videos for the conditions are provided in the following YouTube location and summarized in Table AI.

Appendix A2: Analytical Heat Transfer Model

Thermal cycles under steady-state conditions for the E-PBF process were calculated using the following equation, which is indeed a derivative of the classic formulism developed by Rosenthal.[42] This equation was used for estimating the thermal distribution during E-PBF by Sames *et al.*[24]

$$T = T_0 + \frac{\eta Q/V}{2\pi\lambda\sqrt{t(t+t_0)}}\exp\left\{-\frac{1}{4a}\left[\frac{(z+z_o)^2}{t}+\frac{(y)^2}{t+t_0}\right]\right\}. \quad [A1]$$

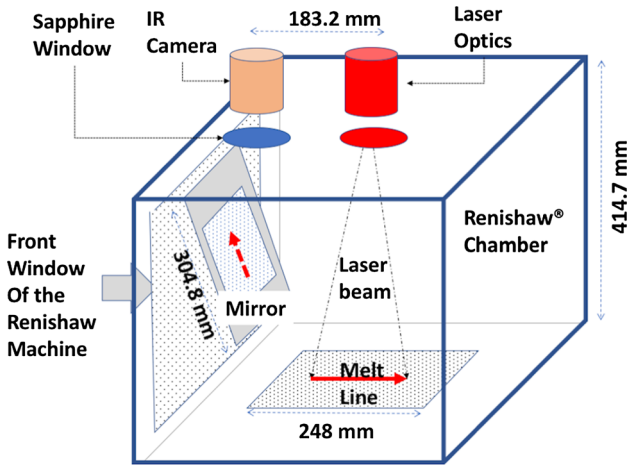

Fig. A1—Schematic illustration of the IR imaging setup used in the current investigation.

In the above equation, T_0 is the preheat temperature (443 K), Q is the heat input (200 W), V is the scan velocity, t is the time in seconds, y is the distance perpendicular to the beam direction, z is the distance along the thickness of the powder bed or solid, a_o is the thermal diffusivity, t_0 is the characteristic time given by the equation $(r_b^2/4a)$, r_b is the radius of the heat source (35 μm), and z_o is the characteristics thickness given by the equation $\left(\left[((r_b/e)/(\pi a r_b/V))^{0.5}\right]\right)$. The following parameters (Table AII) were used for calculation of thermal distribution shown in the main text. While calculating thermal distribution for the 100 pct powder bed condition (no solid underneath), the powder thermal conductivity was assumed to be 15 pct of the solid nickel.

Appendix A3: Interface Response Function Model

For the benefit of the reader, the salient equations to describe columnar to equiaxed transition (CET) and relevant thermodynamic data for the alloy 718 are based on the classical interface response function developed by solidification researchers.[61,62] The original governing equation for the CET was derived by Gaumann *et al.*[48] to describe the probability of stray grains (ϕ), which is given below:I

$$G = \frac{1}{n+1}\sqrt[3]{\frac{-4\pi N_o}{3\ln(1-\phi)}}\Delta T_c\left(1-\frac{\Delta T_n^{n+1}}{\Delta T_C^{n+1}}\right). \quad [A2]$$

In the above equation, G is the thermal gradient, ΔT_c is the constitutional tip undercooling, n is the power factor, and N_0 is the number density of pre-existing nuclei ahead of the liquid–solid interface. In the above equation, the roles of liquid–solid interface velocity ($R_{L/S}$) and dendrite tip radius (R_{Tip}) are taken care of through a change in the ΔT_c, given by the following equation:

$$\Delta T_c = \sum_{i=1}^{n}\left(c_l^{i*}m_V^i - c_o^i m_o^i\right) - \frac{2\Gamma}{R_{Tip}}. \quad [A3]$$

In the above equation, c_o^i is the nominal concentration of ith element, m_o^i is the equilibrium liquidus slope, m_V^i is the velocity-dependent liquidus slope, c_l^{i*} is the concentration of the ith element at the dendrite tip, and Γ is the Gibbs–Thomson coefficient. The c_l^{i*} can be calculated using the following equation:

$$c_l^{i*} = \frac{c_o^i}{\left[1-\left(1-k_v^i\right)\right]Iv\{Pe\}}. \quad [A4]$$

In the above equation, k_v^i is the partitioning ratio for ith element as a function of liquid–solid interface velocity and $Iv\{Pe\}$ is the Ivantsov function of the Peclet (Pe) number. The Pe is related to the liquid–solid interface velocity ($R_{L/S}$), dendrite tip radius (R_{Tip}), and the diffusivity (D_i) of the ith element in liquid with the following relationship:

Table AI. Links to the Processed IR Image Movies for All the Processing Conditions are Given Below

Condition	Location of the Movie	Condition	Location of the Movie
1	https://youtu.be/Dj9MBXpKOow	26	https://youtu.be/R06Cypa6EeA
2	https://youtu.be/XPG8CbKrj6Q	27	https://youtu.be/aL9nSQBsqkA
3	https://youtu.be/Ex8Xk7-Xzoo	28	https://youtu.be/JQdQlQULP-o
4	https://youtu.be/Sh3owcosH0g	29	https://youtu.be/8ohNnXDTCJQ
5	https://youtu.be/JgZ6VWs7O1U	30	https://youtu.be/lCeVnVscl-E
6	https://youtu.be/ot731ewlkS8	31	https://youtu.be/HNLrlfn1_zU
7	https://youtu.be/LXcq4ReurcA	32	https://youtu.be/EwlGP9ESkbk
8	https://youtu.be/4yvOuep7ilc	33	https://youtu.be/wrsfaa48bRU
9	https://youtu.be/597HPqS6eBc	34	https://youtu.be/RPZmSk3480g
10	https://youtu.be/CK48-qUZUKU	35	https://youtu.be/UGaJrBKSgas
11	https://youtu.be/xwfAJS9MDo8	36	https://youtu.be/QlZ46yoPxVc
12	https://youtu.be/VSwRlYBBEWg	37	https://youtu.be/Hd7fUVBQ_iw
13	https://youtu.be/apAyPXKsFkw	38	https://youtu.be/lT8DrSLBN4c
14	https://youtu.be/pIQ7aA97wuI	39	https://youtu.be/IMuAFSS4110
15	https://youtu.be/AxAM4zh2aCk	40	https://youtu.be/gRPqWSXPQns
16	https://youtu.be/YYMOZGTDWxo	41	https://youtu.be/4e0KEjOl2Ss
17	https://youtu.be/oZaHtvmFa6g	42	https://youtu.be/mqwL6-z9uF4
18	https://youtu.be/imfKvY3lJGU	43	https://youtu.be/sk-JXMdD_N0
19	https://youtu.be/JIVd9V0fnQk	44	https://youtu.be/vnllBPGuxck
20	https://youtu.be/FFywGt5Magw	45	https://youtu.be/NjTbZn2B4ns
21	https://youtu.be/-LSV0VI7nfw	46	https://youtu.be/izhW_Z-stM8
22	https://youtu.be/4N_xVdlC4N8	47	https://youtu.be/9zpXPXAtDAs
23	https://youtu.be/KnvuDvCYaWg	48	https://youtu.be/Vw38YNcHPu4
24	https://youtu.be/33UjhIm-dIY	49	https://youtu.be/IJE4tCsLpmU
25	https://youtu.be/YmZhRzsvNYI		

Table AII. Physical Parameters Used for the Thermal Analysis of Relevant Nickel Alloys

Parameter	Value	Remarks
Specific heat (C_p)	0.435 J/(g K)	no temperature dependence
Density (ρ)	8.19×10^6 g/m^3	no temperature dependence
Thermal conductivity	11.2 W/m/K	no temperature dependence

$$Pe = \frac{R_{Tip} R_{L/S}}{2D_i}. \quad [A5]$$

Furthermore, the velocity-dependent partitioning (k_v^i) is related to the equilibrium partitioning ratio (k_o^i) and the characteristic diffusion distance (a_0) through the following relationship derived by Aziz[44]:

$$k_v^i = \frac{k_o^i + a_0\left(R_{L/S}/D_i\right)}{1 + a_0\left(R_{L/S}/D_i\right)}. \quad [A6]$$

Similarly, the liquid slope (m_V^i) is given by the following relationship:

$$m_v^i = m_o^i\left[\frac{1 - \left(1 - \ln\left(k_v^i/k_o^i\right)\right)}{1 - k_o^i}\right]. \quad [A7]$$

The only other unknown in the above formulation is the dendrite tip radius (R_{Tip}), which is described by the well-known interface instability criteria given below:

$$\left(4\pi^2\Gamma\frac{1}{R_{Tip}^2}\right) + \left(2\sum_{i=1}^{n}\left\{m_v^i P_e^i\left(1 - k_v^i\right)\left[c_l^{i*}\zeta_c^i\right]\right\}\frac{1}{R_{Tip}}\right) + (G) = 0. \quad [A8]$$

With the above Eqs. [A3] through [A7] and thermodynamic data from CALPHAD techniques,[45,63] it is possible to construct the solidification maps for any alloy composition. The data used for the calculations are summarized in Table AIII.

Appendix A4: Simultaneous Transformation Kinetics Model

In all the computational weld mechanics modeling or additive manufacturing, it is important to describe the solid-state phase decomposition of the parent phase (γ) to different product phases (γ' and/or γ'', Laves, MX and δ phase) during repeated heated and cooling in the

Table AIII. Parameters Used for the Interface Response Function Calculations (Rounded to Two Decimal Points)

Element ID	Comp. (At. Pct)	k_o^i	m_o^i	Parameters	value
Al	1.27	1.16	− 5.76	a_0 (m)	3.0×10^{-10}
Cr	20.09	1.07	− 2.63	n	3.4
Fe	18.13	1.19	− 1.04	N_o m^{-3}	varied
Mo	1.77	0.65	− 6.35	Γ (m K)	3.37×10^{-7}
Nb	3.20	0.20	− 14.36	ϕ	varied from 0 to 1
Ti	1.03	0.40	− 15.19	liquidus (K)	1611.02
C	0.16	0.13	− 10.70	solidus (K)	1530.56
Ni	54.01	1.02	1.04	D_i (m^2/s)	5.0×10^{-9}
O	0.04	0.25	− 3.66	ΔT_n	3.5
Si	0.19	0.64			
Co	0.11	1.05			

Table AIV. Calibration Parameters for the STK Model Relevant to the Current Research

Phases	DED Values (Makiewicz *et al.*)	New Calibration (Current Work)
Pre-exponent nucleation factor: mm^{-3}s^{-1}		
γ	2.5×10^{16}	1×10^{19}
γ''	2.5×10^{15}	1×10^{18}
MX	1×10^{15}	1×10^{15}
Laves	1×10^{5}	1×10^{5}
δ	1×10^{10}	1×10^{10}
γ''	0.095	0.095
Surface energy parameter (σ) J/m^2		
For all phases	0.095	0.095
Growth acceleration parameter $(\chi_{\gamma'})$		
For all phases	1	1
MX	3	3

solid-state. In this regard, the simultaneous transformation kinetics (STK) modeling framework development by Jones and Bhadeshia[64] can be adopted. This model can consider competition between individual precipitates when calculating the nucleation and growth rates based on the assumptions made for JMAK theory,[65] in a discrete fashion. Makiewicz *et al.*[60] extended this formulism to additive manufacturing of Inconel 718 alloys. Although the details of this theoretical formulism are outlined by Makiewicz *et al.*,[60] the methodology is briefly described below for context. In order to describe the phase transformations that occur in any arbitrary thermal cycle that involves multiple heating and cooling modes, the whole cycle is subdivided into smaller isothermal steps at a given temperature. The model takes the initial microstructure (*e.g.*, $v_{\gamma'}^i$, volume fraction of phase) at $(i-1)$th time step, before entering ith time step (dt) at a given temperature and calculates the change of the fraction depending on the volume fraction of all the other phases.

$$dv_{\gamma'}^i = \left(1 - \frac{\left[v_n^{i-1} - \sum_n^{n=k} dv_n^i\right]}{v_{\gamma'}^{i-1}}\right) dv_{\gamma'(\text{ext})}^i\Big|_{n\neq\gamma'} \qquad [A9]$$

In the above equation, $dv_{\gamma'(\text{ext})}^i$ is the change in extended volume of the γ' phase given by the following equation, by assuming spherical precipitates:

$$dv_{\gamma(\text{ext})}^i = \left(\frac{4}{3}\pi\left[G_3^*\left(\sqrt{t-\tau}\right)\right]^3\right) I_v dt \qquad [A10]$$

In the above equation, I_v is the nucleation rate, G_3^* is the growth rate, t is the equivalent time, and τ is the incubation time at that given temperature. The I_v for each phase can be calculated using a generic equation given below:

$$I_v = I_o \exp\left\{\frac{-Q_{\text{act}}}{kT}\right\}, \qquad [A11]$$

where $Q_{\text{act}} = \frac{16\pi\sigma^3}{3\Delta G_v^2}$ is the activation energy for nucleation, which is a function of interfacial energy (σ) and the maximum driving force (ΔG_v) for nucleation. This driving force can be calculated using ThermoCalc® software.[47] The growth rate of each phase can be calculated using the following equation, which relates the supersaturation and the growth rate (G_3^*), assuming no soft impingement. The typical equation for the γ' is given below:

$$G_3^* = \chi_{\gamma'} \frac{(x_o - x_\gamma)}{2(x_{\gamma'} - x_\gamma)} \sqrt{\frac{D}{t}}. \quad [A12]$$

The supersaturation term in the above equation is related to the bulk concentration of principal element (x_o) controlling the diffusion-controlled growth of γ', x_γ is the interface concentration at the FCC matrix, and $x_{\gamma'}$ is the interface concentration of γ. The $\chi_{\gamma'}$ is the empirical acceleration parameter used to throttle down or up certain precipitates. Makiewicz *et al.*[60] used experimental data from a laser powder blown deposition process (DED) to calibrate these parameters (see Table AIV). We have adopted the above methodology to rationalize the solid-state decomposition during the Gleeble® thermal simulations. The STK model requires sixteen parameters as inputs, however, the calibrations developed for the DED process underestimated the precipitation volume fractions of γ' and γ'' with reference to the controlled Gleeble® simulated thermal gyration experiments and, also, published data from EBM builds.[35] To correct these underestimations, a new set of calibration parameters was developed (see Table AIV).

REFERENCES

1. R.A. Roach and S.H. Gardner: *Transl. Mater. Res.*, 2017, vol. 4, p. 044001.
2. M. Seifi, M. Gorelik, J. Waller, N. Hrabe, N. Shamsaei, S. Daniewicz, and J.J. Lewandowski: *JOM*, 2017, vol. 69, pp. 439–55.
3. B.H. Jared, M.A. Aguilo, L.L. Behini, B.L. Boyce, B.W. Clark, A. Cook, B.J. Kaehr, and J. Robbins: *Scripta Mater.*, 2017, vol. 135, pp. 141–47.
4. NIST: Measurement Science Roadmap for Metal-based Additive Manufacturing, prepared by Energetics Incorporated, 2013. http://www.nist.gov/el/isd/upload/NISTAdd_Mfg_Report_FINAL-2.pdf.
5. S.K. Everton, M. Hirsch, P. Stravroulakis, R.K. Leach, and A.T. Clare: *Mater. Des.*, 2016, vol. 95, pp. 431–45.
6. H. Krauss, C. Eschey, and M.F. Zaeh: *Proc. 23rd Annu. Int. Solid Free. Fabr. Symp.* 2012, pp. 999–1014, https://doi.org/10.1017/cbo9781107415324.004.
7. S. Clijsters, T. Craeghs, S. Buls, K. Kempen, and J.P. Kruth: *Int. J. Adv. Manuf. Technol.*, 2014, vol. 75, pp. 1089–1101.
8. R.B. Dinwiddie, R.R. Dehoff, P.D. Lloyd, L.E. Lowe, and J.B. Ulrich: *Thermosense*, 2013, vol. 8705, pp. 1–9.
9. R.B. Dinwiddie, M.M. Kirka, P.D. Lyod, R.R. Dehoff, L.E. Lowe, G.S. Marlow: *Proc. SPIE*, 2016, Vol. 9861. https://doi.org/10.1117/12.2229070.
10. S. Moylan, E. Whitenton, B. Lane, and J. Slotwinski: *40th Annu. Rev. Prog. Quant. Nondestruct. Eval., AIP Conf. Proc.* 2014, Vol. 1581, pp. 1191–96. https://doi.org/10.1063/1.4864956.
11. G. Marshall, W.J. Young II, N. Shamsaei, J. Craig, T. Wakeman, and S.M. Thompson: *Proc. Solid State Free Form.* 2015, pp. 259–72. https://sffsymposium.engr.utexas.edu/sites/default/files/2015/2015-21-Marshall.pdf.
12. E. Rodriguez, J. Mireles, C. Terrazas, D. Espalin, M. Perez, and R.B. Wicker: *Addit. Manuf.*, 2015, vol. 5, pp. 31–39, https://doi.org/10.1016/j.addma.2014.12.001.
13. M. Doubenskaia, M. Pavlov, S. Grigoriev, and I. Smurov: *Surf. Coatings Technol.*, 2013, vol. 220, pp. 244–47, https://doi.org/10.1016/j.surfcoat.2012.10.044.
14. G. Bi, A. Gasser, K. Wissenbach, A. Drenker, and R. Poprawe: *Opt. Lasers Eng.*, 2006, vol. 44, pp. 1348–59, https://doi.org/10.1016/j.optlaseng.2006.01.009.
15. P. Lott, H. Schleifenbaum, W. Meiners, K. Wissenbacj, C. Hinke, and J. Bultmann: *Phys. Procedia*, 2011, vol. 12, pp. 683–90.
16. W.S. Land, II, B. Zhang, J. Ziegert, and A. Davies: *Procedia Manuf.*, 2015, vol. 1, pp. 393–403.
17. S. Huber, J. Glasschroeder, and M.F. Zaeh: *Phys. Procedia*, 2011, vol. 12, pp. 712–19.
18. L. Mrna and M. Sarbort: *Phys. Procedia*, 2014, vol. 56, pp. 1261–67.
19. M. Schwalbe: Predicting theoretical and computational approaches for additive manufacturing. *Proc. Workshop Natl. Acad. Sci.*, 2016.
20. ISO/ASTM 52900:2015(E): Standard terminology for additive manufacturing – General principles – Terminology, ASTM International, 2016.
21. I. Yadroitsev, A. Gusarov, I. Yadroitdave, and I. Smurov: *J. Mater. Process. Technol.*, 2010, vol. 210, pp. 1624–31.
22. I. Yadroitsev and I. Smurov: *Phys. Procedia*, 2010, vol. 5, pp. 551–60.
23. S. Tammas-Williams, H. Zhao, F. Leonard, F. Derguti, I. Todd, and P.B. Prangnell: *Mater. Charact.*, 2015, vol. 102, pp. 47–61.
24. W. Sames, F.A. List, S. Pannala, R.R. Dehoff, and S.S. Babu: *Int. Mater. Rev.*, 2016, vol. 61, pp. 315–60.
25. S.S. Babu: in *Introduction to Integrated Weld Modeling. ASM Handbook*, D.U. Furrer and S.L. Semiatin, eds., ASM International, 2010, vol. 22B.
26. S. Yoder, S. Morgan, E. Barnes, C. Kinzy, P. Nandwana, M. Kirka, S.S. Babu, V. Paquit, and R.R. Dehoff: *Addit. Manuf.*, 2018, vol. 19, pp. 184–96.
27. A. Plotkowski, M.M. Kirka, and S.S. Babu: *Addit. Manuf.*, 2017, vol. 18, pp. 256–68.
28. N. Raghavan, A. Plotkowski, R.R. Dehoff, J.A. Turner, M.K. Kirka, and S.S. Babu: *Acta Mater.*, 2017, vol. 140, pp. 375–87.
29. Z.C. Cordero, R.B. Dinwiddie, and R.R. Dehoff: *J. Mater. Sci.*, 2017, vol. 52, pp. 3429–35.
30. N. Raghavan, S.S. Babu, R.R. Dehoff, S. Pannala, S. Simunovic, M.K. Kirka, J. Turner, and N. Carlson: *Acta Mater.*, 2016, vol. 112, pp. 303–14.
31. J. Raplee, A. Plotkowski, M. Kirka, R. Dinwiddie, A. Okello, R.R. Dehoff, and S.S. Babu: *Sci. Rep.*, 2017, vol. 7 (4355), p. 4, https://doi.org/10.1038/srep43554.
32. I. Yadroitsev and I. Smurov: *Phys. Procedia*, 2011, vol. 12, pp. 264–70.
33. M. Groeber, E. Schwalbach, W. Musinski, P. Shade, S. Donegan, M. Uchic, D. Sparkman, T. Turner, and J. Miller: *JOM*, 2018, vol. 70, pp. 441–44.
34. W. Sames, K. Unocic, G. Helmreich, S.S. Babu, R. Dehoff, and F. Medina: *Addit. Manuf.*, 2016, vol. 13, pp. 156–65.
35. W. Sames, K. Unocic, R.R. Dehoff, T. Lolla, and S.S. Babu: *J. Mater. Res.*, 2014, vol. 29, pp. 1920–30.
36. Y. Ogawa: *Sci. Technol. Weld. Join.*, 2011, vol. 16, pp. 33–43.
37. S. Tsukamoto: *Sci. Technol. Weld. Join.*, 2011, vol. 16, pp. 33–43.
38. R.R. Dehoff, W.J. Sames, M.K. Kirka, H. Bilheux, A.S. Tremsin, and S.S. Babu: *Mater. Sci. Technol.*, 2015, vol. 31, pp. 931–38.
39. J. Gockel and L. Sheridan: S. P, Barra, N. W. Klingbeil*J. Beuth JOM*, 2017, vol. 69, pp. 2706–10.
40. C.R. Clymer, J. Cagan, and J. Beuth: *J. Mech. Des.*, 2017, vol. 139, p. 100907.
41. M. Tang, P.C. Pistorious, and J.L. Beuth: *Addit. Manuf.*, 2017, vol. 14, pp. 39–48.
42. D. Rosenthal: *Weld. J.*, 1941, vol. 20, pp. 220–34.
43. P.W. Fuerschbach: *Weld. J.*, 1996, vol. 75, pp. 24s–34s.
44. M.J. Aziz: *J. Appl. Phys.*, 1982, vol. 53, pp. 1158–1168.
45. S.S. Babu, J.W. Elmer, J.M. Vitek, and S.A. David: *Acta Mater.*, 2002, vol. 50, pp. 4763–81.
46. A. Plotkowski, O. Rios, N. Sridharan, Z. Sims, K. Unocic, R.T. Ott, R.R. Dehoff, and S.S. Babu: *Acta Mater.*, 2017, vol. 126, pp. 507–19.
47. J.O. Andersson, T. Helander, L. Hoglund, P.F. Shi, and B. Sundman: *CALPHAD*, 2002, vol. 26, pp. 273–312.
48. M. Gaumann, C. Bezencon, P. Canalis, and W. Kurz: *Acta Mater.*, 2001, vol. 49, pp. 1051–62.
49. M.Y. Krasnoperov, R.R.G.M. Pieters, and I.M. Richardson: *Sci. Technol. Weld. Join.*, 2004, vol. 9, pp. 501–06.
50. S.S. Babu, S.M. Kelly, M. Murugananth, and R.P. Martukanitz: *Surf. Coating Technol.*, 2006, vol. 200, pp. 2663–71.

51. S.S. Babu, R.P. Martukanitz, K.D. Parks, and S.A. David: *Metall. Mater. Trans. A*, 2002, vol. 33A, pp. 1189–1200.
52. C. Villafuerte, H.W. Kerr, and S.A. David: *Mater. Sci. Eng. A*, 1995, vol. 194, pp. 187–91.
53. J.H. Martin, B.D. Yahata, J.M. Hundley, J.A. Mayer, T.A. Schaedler, and T.M. Pollock: *Nature*, 2017, vol. 549, pp. 365–69.
54. O.M. Barabash, S.S. Babu, J.M. Vitek, S.A. David, J.-W. Park, J.A. Horton, G.E. Ice, R.I. Barabash, and J. App: *Physics*, 2004, vol. 96, pp. 3673–79.
55. O.M. Barabash, S.S. Babu, S.A. David, J.M. Vitek, and R.I. Barabash: *J. Appl. Phys.*, 2003, vol. 94 (1), pp. 738–42.
56. P.J. Withers and H.K.D.H. Bhadeshia: *Mater. Sci. Technol.*, 2001, vol. 17, pp. 366–75.
57. D. Wian, J. Xue, A.X. Zhang, Y. Li, N. Tamura, Z. Song, and K. Chen: *Sci. Rep.*, 2017, vol. 7, p. 2859.
58. Y.M. Wang, T. Voisin, J.T. McKeown, J. Ye, N.P. Calta, Z. Li, Z. Zeng, Y. Zhang, W. Chen, T.T. Roehling, R.T. Ott, M.K. Santala, P.J. Depond, M.J. Matthews, A.V. Hamza, and T. Zhu: *Nat. Mater.*, 2018, vol. 17, pp. 63–71.
59. S.S. Babu: in *Proc. Int. Conf. Solid–Solid Phase Transform. Inorg. Mater.* M. Millitzer, G. Botton, L.-Q. Chen, J. How, C. Sinclair, and H. Zurob (eds.) TMS, 2015, pp. 1019–26.
60. K.T. Makiewicz: MS Thesis, The Ohio State University, 2013.
61. S. Fukumoto and W. Kurz: *ISIJ Int.*, 1999, vol. 39, pp. 1270–79.
62. J.A. Dantzig and M. Rappaz: *Solidification*, 2nd ed., EPFL Press, Lausanne, 2016.
63. S.S. Babu: *Int. Mat. Rev.*, 2009, vol. 54, pp. 333–367.
64. S.J. Jones and H.K.D.H. Bhadeshia: *Acta Mater.*, 1997, vol. 45, pp. 2911–2920.
65. J.W. Christian: *The Theory of Transformations in Metals and Alloys v1 and v2*, Pergamon Press, Oxford, 2002.